Alonso, L., Garcia-Gonzalez, D., Navarro, C. & Garcia-Castillo, S. K. (2021). A non-dimensional theoretical approach to model high-velocity impact on thick woven plates. *Steel and Composite Structures, 38*(6), 717-737.

DOI: 10.12989/scs.2021.38.6.717

Steel and Composite Structures, *Vol. 38, No. 6 (2021) 000-000*
DOI: https://doi.org/10.12989/scs.2021.38.6.000

A non-dimensional theoretical approach to model high-velocity impact on thick woven plates

L. Alonso*[1], D. Garcia-Gonzalez[2], C. Navarro[2] and S.K. García-Castillo[2]

[1]*Department of Chemical Technology, Energy and Mechanics, Rey Juan Carlos University, C/Tulipán s.n., 28933*
[2]*Department of Continuum Mechanics and Structural Analysis, University Carlos III of Madrid, Avda. de la Universidad 30, 28911*

(*Received August 2, 2020, Revised December 24, 2020, Accepted February 19, 2021*)

Abstract. A theoretical energy-based model to capture the mechanical response of thick woven composite laminates, which are used in such applications as maritime or aerospace, to high-velocity impact was developed. The dependences of the impact phenomenon on material and geometrical parameters were analysed making use of the Vaschy-Buckingham Theorem to provide a non-dimensional framework. The model was divided in three different stages splitting the physical interpretation of the perforation process: a first where different dissipative mechanisms such as compression or shear plugging were considered, a second where a transference of linear momentum was assumed and a third where only friction took place. The model was validated against experimental data along with a 3D finite element model. The numerical simulations were used to validate some of the new hypotheses assumed in the theoretical model to provide a more accurate explanation of the phenomena taking place during a high-velocity impact.

Keywords: energy-absorption; impact behavior; analytical modelling; numerical modelling; FRP

1. Introduction

Composite materials are well known for their good mechanical properties as well as their low weight. These two characteristics make them ideal candidates to be used in applications where cost reduction and safety under different mechanical demands are the most important requirements (Kharazan *et al*. 2014, Garcia-Gonzalez *et al*. 2015, Guangyong *et al*. 2018). In fact, optimization processes are common to reduce costs within the field of composite materials (Ehsani and Rezaeepazhand 2016, Costas *et al*. 2017, Dhari *et al*. 2019). These materials are conceived to meet different economical and mechanical requirements but they also need to be able to withstand extraordinary circumstances that may occur during their service life. For instance, high-velocity impact is a common scenario within the aerospace industry (Briescani *et al*. 2015, Pekbey *et al*. 2017, Rodriguez-Millan *et al*. 2018). Moreover, there are other industries such as transport or maintenance where composite materials are likely to suffer accidents. For example, pipes made of E-glass polyester laminates might be subjected to impacts in some environments. In view of these examples, the study of high-velocity impact on composite materials can be considered as a hot topic (Haro *et al*. 2016, Zhang *et al*. 2016, Hazzard *et al*. 2018, Alonso *et al*. 2018a, Sikarwar and Velmurugan 2019, Scazzosi *et al*. 2019, Gil-Alba *et al*. 2019). This problem can be approached by different methodologies: experimental, theoretical and numerical.

Regarding numerical models, different approaches based on the finite element method (FEM) have successfully been applied to simulate the impact phenomenon (Davila *et al*. 2005, Miamí *et al*. 2007, Lopes *et al*. 2009, Yiru Ren *et al*. 2018). More recent numerical models have been developed to capture different effects such as damage modes or the service-life under fatigue tensile loading of 3D braided composites (Ding *et al*. 2018, Chao Zhang *et al*. 2018). Other damage models have recently been developed in composite materials to predict complex phenomena such as fracture in layered structures (Nguyen *et al*. 2019), punch tests (Liu *et al.* 2017) and the evolution of plasticity parameters in FRP-confined concrete structures under compression (Saberi *et al*. 2020). The main advantage of theoretical and analytical models compared to numerical and experimental ones is the saving in time, computational and economic costs. They allow the understanding of the main failure mechanisms involved saving a lot of resources compared to other methodologies (Naik and Doshi 2005).

The prediction of the ballistic behaviour of laminate plates is an important field to be studied due to the high number of engineering applications in which these materials can be useful. The approaches used to formulate analytical and theoretical models, can be mainly divided into those based on energetic considerations and those based on momentum transfer. Related to the latter, several authors have developed models based on the transfer of linear momentum between the projectile and the laminate layers (Mamivand and Liaghat 2010, Briescani *et al*. 2015). The model proposed in this paper is developed combining these two approaches. Its formulation is based on energetic criteria and accounts, at the same time, for the transfer of linear momentum within the energy-absorption mechanisms

*Corresponding author, Ph.D.
E-mail: luis.alonso.sanjose@urjc.es

http://www.techno-press.org/?journal=scs&subpage=8
ISSN: 1229-9367 (Print), 1598-6233 (Online)

(thus creating a new branch in this classification). Another classification can be based on specimen thickness so that the models can be divided into those with thin or thick laminates. However, there is no clear threshold in the literature for this classification. In the study performed by Alonso *et al*. (2018a), a threshold was proposed for GFRP plates, but further efforts are needed to provide a more accurate criterion.

Regarding thin composite laminate modelling based on energetic criteria, its evolution has been remarkable over recent years. Zhu *et al*. (1992) developed an analytical model for Kevlar 29/polyester targets. This model is divided into three stages: indentation, perforation and exit. Different energy-absorption mechanisms such as fibre failure or friction are taken into account and the laminated plate theory is used. Navarro (1998) stated that models of brittle composite materials should be different from ductile composite materials because of the energy-absorption mechanisms involved. Furthermore, this author developed an analytical model applying the one-dimensional elastic wave theory. The analytical model for polymer composites proposed by Moyre *et al*. (2000) considers the energy absorbed by the laminate divided into kinetic energy transferred to the laminate, elastic deformation of fibres and tensile failure of fibres, while obtaining an analytical expression for the ballistic limit velocity. Naik and Shrirao (2004), Naik *et al*. (2006) developed a model for woven fabric composites. This model is based on an energy balance taking into account delamination, matrix cracking, shear plugging, elastic deformation of fibres, tensile failure of fibres and the kinetic energy transferred from the projectile to the laminate. This model is formulated incrementally, where time is divided in small increments and the kinematic variables are calculated in each step. García-Castillo *et al*. (2012) developed a theoretical model based on an energy balance which leads to a differential equation solved by numerical methods.

Moreover, the literature is less extensive regarding thick composite laminate modelling based on energetic criteria. Naik and Doshi (2005) formulated a model for thick woven composites taking into account wave propagation through the thickness direction and additional energy-absorption mechanisms taking place (compression). These authors divided the impact event into three stages associated with different energy-absorption mechanisms. Wen (2000, 2001) developed an analytical model for the penetration and perforation of thick FRP laminates struck by projectiles with different nose shapes such as flat, conical or truncated cone. This model is formulated by means of the resistive pressure and the dynamic resistive pressure. Alonso *et al*. (2018a) developed another theoretical model for thick laminates of GFRP plates taking into account the same mechanisms as Naik and Doshi (2005). However, this model is limited to two stages and some improvable simplifications are assumed in the perforation process. The proposed model is divided into three stages according to new experimental observations (Gil-Alba *et al*. 2019). The experimental study for thick laminates carried out by the authors in previous works strongly suggested that the transition between stages is related to the change in the morphological shape of damage after a certain depth. This depth matches the compressive out-of-plane failure strain.

The main objective of this work is to characterise and model the response of thick GFRP plates subjected to high-velocity impact. To achieve this goal, a non-dimensional energy-based theoretical model, which is divided into three different stages, is formulated. This model assumes physically motivated hypotheses such as the profile of velocities across thickness and the instantaneous transfer of linear momentum in the second stage, combining two of the current existent approaches. It also gives information about the relative importance of the different energy-absorption mechanisms in the three stages. The theoretical model is validated against experimental results. Moreover, original tests were performed to obtain out-of-plane properties of the laminates. Furthermore, other important hypotheses such as the failure mode determining the transition between the first two stages are supported in previous experimental observations. Finally, a 3D finite element model, which was validated against experimental results (Alonso *et al*. 2020), is used as a reference for the comparison with the energy-absorption results given by the theoretical model. Moreover, the FEM model is also used to validate some of the novel hypotheses incorporated in the theoretical model.

2. Material characterisation

2.1 Material description

Characterisation tests on woven E-glass/polyester plates were conducted in this work. These laminates were already well characterised in previous studies carried out by García-Castillo *et al*. (2006), Buitrago *et al*. (2010) and Alonso *et al*. (2018a). Table 1 shows the static properties obtained in those previous works. The dynamic values used at high-strain rates, also shown in Table 1, were taken from the static properties as proposed by Alonso *et al*. (2020) in the theoretical model.

Nevertheless, some properties that were estimated from other works such as the Young's modulus or the failure compressive stress in the thickness direction needed to be revisited.

2.2 Out-of-plane compression tests

The objective of the compression tests was to determine the Young's modulus and the compressive failure stress and strain in the thickness direction.

In order to design the procedure for this test, ASTMStandard-D695-96 (1995), indicated to determine the compressive failure stress for composite specimens, was followed. Prevention of bending, Euler buckling and barrel effects was ensured during the tests.

The cube dimensions of the specimens were 12 mm x 12 mm x 12 mm. A set of five tests was carried out to ensure repeatability. This geometry was previously used by Tarfaoui *et al*. (2008) to measure similar properties at different strain rates in GFRPs samples.

Table 1 Summary of the static properties of woven E-glass fibre/polyester laminates obtained by García-Castillo *et al*. (2006), Buitrago *et al*. (2010), Alonso *et al*. (2018a, 2020).

Property	Nomenclature	Quasi-static Value	Dynamic Value
Laminate density [Kg.m^3]	ρ_l	1980	1980
Young's modulus in directions 11 and 22 [GPa]	$E_{11} = E_{22}$	10.1	15.2
Shear modulus in direction 12 [GPa]	G_{12}	4.4	6.5
Poisson's coefficient	$\nu_{12} = \nu_{23} = \nu_{31}$	0.16	0.16
Failure stress in directions 11 and 22 [MPa]	$X_{11_t} = X_{22_t}$	367	1102
Failure shear stress in directions 12, 23 and 13 [MPa]	$S_{12} = S_{23} = S_{13}$	136	204
Shear modulus in directions 23 and 13 [GPa]	$G_{23} = G_{13}$	0.48	0.72
Compressive failure strength in directions 11 and 22 [MPa]	$X_{11_c} = X_{22_c}$	309	928
Shear failure matrix strength in directions 12, 23 and 13 [MPa]	$S_{12_s} = S_{23_s} = S_{13_s}$	120	180

(a)

(b)

Fig. 1 (a) 8802 INSTRON universal test machine connected to the out-of-plane compression tool. (b) Specific device for the out-of-plane compression tests with a specimen already tested

To perform these tests in optimal conditions, we used an specific device that fitted into the 8802 INSTRON machine (see Fig. 1(b)). The compression disks were cubes of 50 mm x 50 mm x 50 mm made of hardened steel with 54 HRC hardness. This hardness was enough to ensure that there was no deformation in the disks during the tests. Furthermore, the upper disk had a small pinned joint so that the possible manufacturing defects could be balanced and the load was always applied parallel to the surface. These characteristics made the performance of the tests possible. The tests were performed with a velocity of 1 mm min^{-1} as proposed by ASTM-Standard-D695-96 (1995) to ensure quasi-static conditions during the test.

As shown in Fig. 1b, the breakage shape was conical as expected for laminates similar to E-glass fibre/polyester. For example, Ferguson *et al*. (1998) predicted a similar breakage shape for 0/90 woven glass/epoxy laminates.

Assuming uniaxial conditions, the stress-strain curve along the thickness direction can be represented from the data recorded. To this end, stress and strain were calculated with Eqs. (1) and (2).

$$\sigma_3 = \frac{F_c}{A_c} \tag{1}$$

$$\varepsilon_3 = \frac{x}{L_0} \tag{2}$$

where A_c is the area in contact with the steel disk (12 mm x 12 mm), $F_c$is the force recorded by the machine, L_0 is the initial thickness of the laminate (12 mm) and x is the displacement of the machine in a reference system with origin in the starting test position.

Fig. 2 shows the mean stress-strain curve of the tests. The relationship between these variables was found to be linear until failure (R^2=0.9926).

The slope of this curve represents the compressive Young's modulus along the thickness direction. Moreover, the stress before failure can be interpreted as the compressive failure stress along the thickness direction. These values are estimated, as a first approach, following the procedure presented by Alonso *et al*. (2020), see Table 2.

2.3 Friction curves

The main goal of the friction tests was to motivate the modelling of the advance of the projectile during the perforation stage. To this end, force-displacement curves

Table 2 Static properties of woven E-glass fibre/polyester laminates determined by out-of-plane compression tests as per ASTM-Standard-D695-96 (1995)

Property	Nomenclature	Quasi-static Value	Dynamic Value
Compressive Young's modulus in direction 33 [GPa]	E_{33}	4.5	6.75
Compressive failure stress in direction 33 [MPa]	X_{33}	464	1392
Compressive failure strain in direction 33	ε_{3_c}	0.1085	0.217

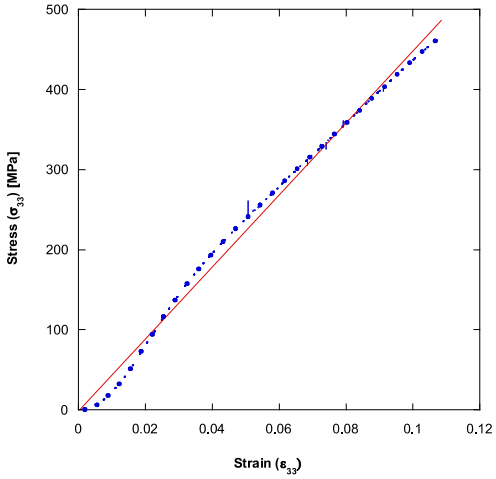

Fig. 2 Mean out-of-plane compressive stress (σ_{33}) vs strain (ε_{33}) curve along the thickness direction obtained from the out-of-plane tests

were used to compute the energy absorbed by friction. To perform these tests in optimal conditions, we followed ASTM-Standard-D732-02 (2002) as proposed by other authors for friction tests (Pandya *et al*. 2015). We performed the tests following this procedure and using the specimen geometry (50 mm x 50 mm) described by Alonso *et al*. (2018a).

The schema of the relative disposition during the test between the specimen and the machine can be seen in Fig. 3. The friction punch was placed in the upper jaw of the universal testing machine. The concavity of the punch was located on the projectile ensuring contact so that the punch guided the movement. Once the test started, the lower stem moved up with a velocity of 1 mm min^{-1} while the punch was fixed (ASTM-Standard-D732-02, 2002).

The data related to the tests performed are collected in Table 3.

The results show almost perfect repeatability, providing clear representative curves for 9 mm thickness and 12 mm thickness tests. An adjustment by means of least squares provided the analytical equations with their valid intervals of applications to be used in the theoretical model. The analytical expressions for the friction force have a fit coefficient greater than 0.98.

$$F = \begin{cases} 0.4569x + 0.1014, & if \;\; 0 < x \leq 1.17 \\ 3.1815x - 2.743, & if \;\; 1.17 < x \leq 3.72 \\ 0.1002x^2 - 2.624x + 16.952, & if \;\; 3.72 < x \leq 9 \end{cases} \quad (3)$$

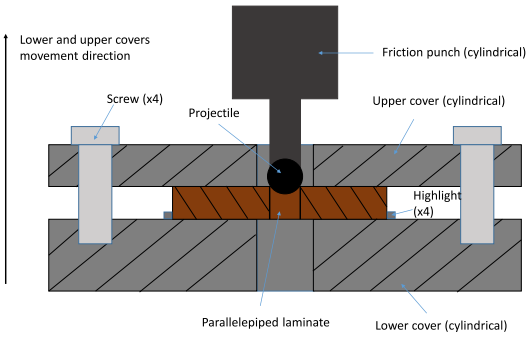

Fig. 3 Relative disposition between the laminate and the test machine at the beginning of the friction tests as per ASTM-Standard-D732-02 (2002)

$$F = \begin{cases} -0.094x^2 + 0.5304x + 0.067, & if \;\; 0 < x \leq 2.68 \\ 4.1184x - 10.264, & if \;\; 2.68 < x \leq 5.60 \\ 0.112x^2 - 3.810x + 30.683, & if \;\; 5.60 < x \leq 12 \end{cases} \quad (4)$$

where x is the spatial coordinate in mm with the origin on the front face of the laminate and F is the friction force in kN. Eqs. (3) and (4) are valid for 9 mm and 12 mm thick specimens respectively.

For both thicknesses, the force increased initially until the projectile was inside the laminate. At this point, the contact surface between the projectile and the laminate reached a maximum. When the projectile began to come out of the specimen by the rear face, the friction force started to decrease. The peak that Eqs. (3) and (4) present for 12 mm thick specimens was higher than the one for 9 mm thick. This is explained by the fact that the larger the thickness the more time the projectile remains inside the laminate.

Pandya *et al*. (2015) carried out similar experiments with E-glass fibre/epoxy laminates. The shape of the curve of these experiments was different compared to Pandya *et al*. (2015) due to the geometry of the projectile. In the tests carried out by Pandya *et al*. (2015) they used a cylindrical flat-ended projectile. Therefore, the contact area between the projectile and the laminate was always growing monotonously and so did the force-displacement adjusted equation.

Friction is a really complicated phenomenon due to the microscopic processes taking place at the same time such as the micro welds between the two bodies (Braun and Naumovets 2005, Li *et al*. 2017), which are a current topic of discussion in the scientific community. Therefore, we are aware that the friction response might be affected by factors

Table 3 Friction test data

Nº Experiments	Thickness [mm]	Projectile diameter [mm]	Hole diameter [mm]	Penetration
6	9	7.5	7.4	Full
7	12	7.5	7.4	Full

such as temperature or sliding velocity. Nevertheless, these tests are considered here as a good approximation as a first approach.

3. Theoretical model

This section presents the theoretical model developed for predicting the performance of thick woven GFRP plates under high-velocity impact. This model is formulated within an energy-based framework that assumes the kinetic energy of the projectile to be absorbed by the laminate in three different stages. First, the main hypotheses are introduced and, then, the energy-absorption mechanisms are described for each stage along with the kinematics.

3.1 Description of the hypotheses and parameters of the model and wave propagation

The theoretical model for thick woven laminates is motivated by previous models developed by Naik and Doshi
(2005) and Alonso *et al*. (2018a). However, the model of Alonso *et al*. (2018a) only predicted the ballistic limit. New considerations have been made to reformulate the whole problem.

The problem depends on three elemental magnitudes which are mass [M], length [L] and time [T]. Nevertheless, this model has three independent stages. The outputs of each stage are taken as inputs for the following stage. Therefore, each stage has been formulated in a non-dimensional form by means of the Vaschy-Buckingham Theorem with its characteristic parameters.

The following hypotheses taken from Alonso *et al*. (2018a) have been assumed in the model formulation:

- Based on experimental evidence (Buitrago *et al*. 2010, Alonso *et al*. 2018a), the projectile is assumed to be rigid and thus it remains undeformed during the entire impact process.
- The mechanical performance of the laminate is considered linear-elastic and x-axially symmetric, where x is the thickness direction.
- The waves considered are the transverse and longitudinal waves (in-plane) and the compressive wave (out-of-plane). All of them remain constant during the impact process.
- In the first stage, the energy absorbed by compression is split into two regions (Fig. 4): the fibres that are directly under the projectile; and the other fibres indirectly affected by the movement of the projectile.
- The energy absorbed by heat transfer between the projectile and the laminate is assumed to be negligible.

Moreover, the following new hypotheses have been incorporated in the formulation of this new model:

- The impact event is divided into the three stages.
- The first stage ends when the complete failure of the laminate takes place. The failure criterion which determines the transition between the first two stages is assumed to be compression. Experimental evidence backs up this hypothesis (Gil-Alba *et al*. 2019).
- The second stage is assumed to be instantaneous and concludes when the transfer of momentum between the projectile and the laminate is completed.
- The third stage only takes into account the friction between the projectile and the laminate, finishing when the projectile exits the laminate. Temperature and sliding velocity are not taken into account.
- The shape of the projectile is considered in the model formulation.

Furthermore, other more specific hypotheses have been added in the three stages and are explained in the following sections. The first stage starts when the projectile impacts the plate. From this moment, several waves propagate in different directions. In-plane longitudinal and transverse waves as well as compressive waves along the thickness direction are considered. Therefore, during this stage different energy-absorption mechanisms are considered: compression, tensile failure of fibres, shear plugging, transference of kinetic energy, matrix cracking and delamination. This stage ends when the complete failure of the laminate takes place. At that moment, a plug with a certain kinetic energy is formed. In the second stage, which is assumed to be instantaneous, the projectile transfers linear momentum to the plug in order to move both bodies at the same velocity. A perfectly inelastic shock between the projectile and the plug is assumed in order to obtain this velocity. With both bodies moving at the same velocity, the third stage starts. In this last stage, only the friction between the projectile and the laminate, experimentally obtained, is taken into account.

In the following sections, all the stages are fully described.

3.2 Stage 1

In the first stage, mass, length and time may be written in their non-dimensional form as follows:

$$[M] = \rho_p \phi_p^3 \tag{5}$$

Table 4 Summary of the parameters and Π groups of the first stage

Parameter	Nomenclature	Value	Π group
Projectile diameter	ϕ_p	7.5 [mm]	
Projectile density	ρ_p	7809 [kg.m^{-3}]	
Impact velocity	v_i [m.s]		
Laminate thickness	e		$\Pi_e = \frac{e}{\phi_p}$
In-plane Young's modulus	E	15.2 [GPa]	$\Pi_E = \frac{E}{\rho_p v_i^2}$
Compressive out-of-plane Young's modulus	E_c	6.75 [GPa]	$\Pi_{E_c} = \frac{E_c}{\rho_p v_i^2}$
In-plane failure strain	ε_r	0.0725	ε_r
Compressive out-of-plane failure strain	ε_{rc}	0.217	ε_{rc}
In-plane failure stress	σ_r	1.102 [GPa]	$\Pi_{\sigma_r} = \frac{\sigma_r}{\rho_p v_i^2}$
Out-of-plane failure shear stress	S_{SP}	201.42 [MPa]	$\Pi_{S_{SP}} = \frac{S_{SP}}{\rho_p v_i^2}$
Laminate density	ρ_l	1980 [kg.m^{-3}]	$\Pi_{\rho_l} = \frac{\rho_l}{\rho_p}$
Energy absorbed by matrix cracking per unit volume	E_{MT}	10^6 [J.m^{-3}]	$\Pi_{E_{MT}} = \frac{E_{MT}}{\rho_p v_i^2}$
Critical dynamic-strain energy-release rate in mode II	G_{IICD}	3000 [J.m^{-2}]	$\Pi_{G_{IICD}} = \frac{G_{IICD}}{\rho_p \phi_p v_i^2}$
Shape factor of delamination	α_{DL}	1	α_{DL}
Shape factor of matrix cracking	α_{MC}	1	α_{MC}
Yarn width	B	5 [mm]	$\Pi_B = \frac{B}{\phi_p}$
Stress wave transmission factor	b	0.9	b

$$[L] = \phi_p \tag{6}$$

$$[T] = \frac{\phi_p}{v_i} \tag{7}$$

where ρ_p is the projectile density, ϕ_p is the projectile diameter and v_i is the impact velocity. The non-dimensional time τ is defined as the integration variable.

The problem (in this stage) depends on 17 fundamental parameters, which are reduced to 14. These parameters are presented in Table 4 along with their corresponding Π groups. Note that some of the parameters are already non-dimensional, so the parameter is directly the Π group in those cases.

The nomenclature to indicate the non-dimensional character of the variables is a bar over the variable. The non-dimensional kinematic variables of the problem are: the position $\bar{x}(\tau)$, the velocity $\bar{v}(\tau)$ and the acceleration $\bar{a}(\tau)$ of the projectile.

Since the laminate is thick enough, a membrane response is not appreciated. Instead, the phenomenon of local compression is more evident. Compression is divided into two regions. A first region (Region 1) corresponding to the volume below the projectile where the fibres are compressed from the projectile to the distance travelled by the through-thickness compressive wave. This is the direct compression, which is caused by the movement of the projectile. The second region (Region 2) corresponds to a domain that goes from the perimeter of the projectile to the distance travelled by the transverse wave. This is the indirect compression because it is not caused directly by the projectile but by the transverse wave on the surroundings. As indirect compression, all the thickness is taken into account from the beginning. These two regions can be seen in Fig. 4. In the first region, the induced stresses provoke material failure at some point when the compressive failure strain is reached.

Wave propagation is a crucial aspect in the formulation of the thick laminates model. Applying the one dimensional wave theory, the transverse and longitudinal wave velocities provoked when a fibre is impacted transversely were defined by Smith *et al*. (1958). Due to the nature of thick laminates, the through-thickness compressive wave, which governs the phenomenon of compression, is considered. The expression of the longitudinal, transverse and through-

thickness compressive waves are given by

$$C_{v_l} = \sqrt{\frac{\Pi_E}{\Pi_{\rho_l}}} \tag{8}$$

$$C_{v_t} = \sqrt{(1+\varepsilon_r)\frac{\Pi_{\sigma_r}}{\Pi_{\rho_l}}} - \sqrt{\frac{\Pi_E}{\Pi_{\rho_l}}}\varepsilon_r \tag{9}$$

$$C_{v_{xl}} = \sqrt{\frac{\Pi_{E_c}}{\Pi_{\rho_l}}} \tag{10}$$

where Π_E, Π_{ρ_l}, Π_E, Π_{σ_r} and ε_r are the Π groups related to the in-plane Young's modulus, the laminate density, the out-of-plane Young's modulus, the in-plane failure stress and the in-plane failure strain, respectively. Consequently, the distance travelled by the longitudinal, transverse and through-thickness compressive waves are given by (11), (12), (13).

$$\overline{R_l}(\tau) = C_{v_l}\tau \tag{11}$$

$$\overline{R_t}(\tau) = C_{v_t}\tau \tag{12}$$

$$\overline{R_{xl}}(\tau) = C_{v_{xl}}\tau \tag{13}$$

In the following subsections, the energy-absorption mechanisms considered in this stage are explained and formulated. Fig. 4 shows the variables and parameters involved during this stage at a generic instant of time.

3.2.1 Energy absorbed by compression in Region 1

The energy absorbed by compression in region 1, $\overline{E_{C1}}$, may be calculated as the energy below the compressive stress-strain curve in the thickness direction multiplied by the volume of such region.

$$\overline{E_{C1}}(\tau) = \bar{V}(\tau,\bar{x})\int_0^{\varepsilon_{rc}} \overline{\sigma_c}(\varepsilon_c)d\varepsilon_c \tag{14}$$

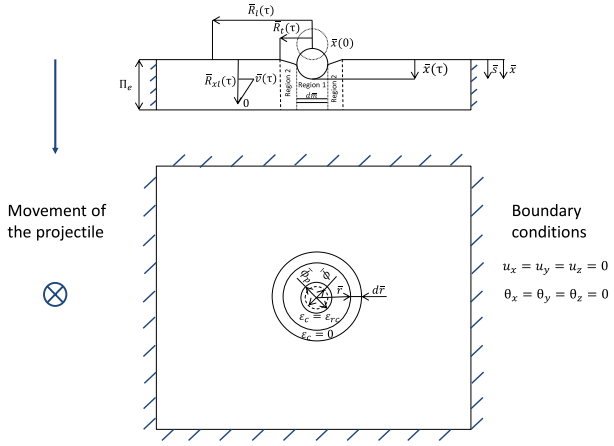

Fig. 4 Schema of the impact phenomenon at a generic instant of time in the first stage representing the variables and parameters involved

where $\bar{V}$, ε_{rc}, $\overline{\sigma_c}$ and ε_c are the affected volume, compressive out-of-plane failure strain, compressive out-of-plane stress and compressive out-of-plane strain respectively. At this point, the definition of the projected diameter in contact with the laminate has to be formulated. In this problem, since the plate does not behave as a membrane due to its thickness, the relative displacement between the projectile and the laminate is considered to be directly the distance travelled by the projectile. Thus, the projected diameter of the projectile can be written as a function of its position

$$\bar{\phi}(\bar{x}) = \begin{cases} 2\sqrt{\bar{x}-\bar{x}^2}, & if\ \ \bar{x} < 0.5 \\ 1, & if\ \ \bar{x} \geq 0.5 \end{cases} \tag{15}$$

The volume of the affected region can be written as

$$\bar{V}(\tau,\bar{x}) = \frac{\pi}{4}\bar{\phi}(\bar{x})^2 C_{v_{xl}}\tau \tag{16}$$

These definitions along with Eq. (14) provide the energy absorbed by compression in region 1.

3.2.2 Energy absorbed by compression in Region 2

Along with the compression below the projectile, there is another region subjected to compression. In its way through the laminate, the projectile provokes the upper fibres to press on the lower fibres generating indirect compression in this zone (see Fig. 4). The energy absorbed by this mechanism is calculated as the area below the compressive stress-strain curve in direction 33 integrated over the volume of the region.

$$\overline{E_{C2}}(\tau) = \int_{\overline{V_0}}^{\bar{V}(\tau)} \left(\int_0^{\varepsilon_r} \overline{\sigma_c}(\varepsilon_c)d\varepsilon_c \right) d\bar{V} \tag{17}$$

where $\overline{V_0}$ is an initial volume and $\bar{V}(\tau)$ is the volume included up to the distance travelled by the transverse wave in the in-plane direction. The compression in this zone is not caused by the compressive wave. On the contrary, it is an indirect compression provoked by the projectile movement and the transverse wave. Then, the expression for the volume differential is the following

$$d\bar{V} = 2\pi\Pi_E \bar{r} d\bar{r} \tag{18}$$

where $\bar{r}$ is the in-plane radial coordinate. Substituting (18) in (17) leads to Eq. (19)

$$\overline{E_{C2}}(\tau) = \pi\Pi_e\Pi_{E_c}\int_{\frac{\bar{\phi}(\bar{x})}{2}}^{\overline{R_t}(\tau)} \varepsilon_c^2 \bar{r} d\bar{r} \tag{19}$$

where Π_e is the Π group related to the thickness of the laminate. The maximum compression is assumed to be reached at the periphery of the projectile and equal to the compressive failure strain through the thickness direction. In addition, we assume that the minimum compression is zero at the radius of the transverse wave. Between these two points, a linear profile of deformations is assumed. Therefore, the deformation is formally defined by (20)

$$\varepsilon_c = \begin{cases} \varepsilon_{rc}, & if\ \ \bar{r} \leq \dfrac{\bar{\phi}(\bar{x})}{2} \\ \dfrac{2(\overline{R_t}(\tau)-\bar{r})}{2\overline{R_t}(\tau)-\bar{\phi}(\bar{x})}\varepsilon_{rc}, & if\ \ \dfrac{\bar{\phi}(\bar{x})}{2} < \bar{r} \leq \overline{R_t}(\tau) \\ 0, & if\ \ \bar{r} \geq \overline{R_t}(\tau) \end{cases} \tag{20}$$

With the profile of deformations defined, the energy absorbed by compression in region 2 is given by Eq. (19).

3.2.3 Energy absorbed by tensile failure of fibres

As the projectile impacts the laminate, compression of the target takes place below the projectile (region 1) and in its surroundings (region 2). As a result of this compression, the fibres which are directly in contact with the projectile are strained in the radial direction (see Fig. 4). Therefore, these fibres may fail as a consequence of the in-plane stress.

An additional hypothesis is needed to quantify the energy absorbed by this mechanism. This hypothesis assumes that the projectile diameter is big enough to impact two perpendicular fibres. These fibres directly impacted by the projectile break with its movement. Consequently, a differential energy as a function of a differential relative displacement, taking into account the fibres affected, can be expressed as

$$d\overline{E_{TF}}(\tau) = 4\Pi_B d\bar{x} \int_0^{\overline{R_l}(\tau)} \left(\int_0^{\varepsilon_a} \bar{\sigma}(\varepsilon) d\varepsilon \right) d\bar{r} \tag{21}$$

where Π_B is the Π group related to the yarn width and ε_a is the attenuated strain defined by the expression proposed by Naik *et al*. (2006)

$$\varepsilon_a = \varepsilon_r b^{\frac{\bar{r}}{\Pi_B}} \tag{22}$$

where b is the stress wave transmission factor. The differential volume considered is defined by the distance travelled by the longitudinal wave, the width of the fibre and the distance travelled by the projectile through the thickness direction.

$$d\bar{V} = 4\Pi_B d\bar{x} d\bar{r} \tag{23}$$

If Eq. (21) is divided by $d\tau$, a linear-elastic behaviour is assumed and the integrals are calculated, Eq. (24), which accounts for the energy absorbed by tensile failure of fibres, is obtained.

$$\overline{E_{TF}}(\tau) = \frac{\Pi_B}{\ln(b)} \Pi_E \varepsilon_r^2 \int_0^{\tau} \left[b^{\frac{2C_{v_l}\tau}{\Pi_B}} - 1 \right] \bar{v}(\tau) d\tau \tag{24}$$

3.2.4 Energy absorbed by transfer of kinetic energy

To better understand the kinetic energy transfer, a comparison with thin laminates can be enlightening. During a high-velocity impact in a thin GFRP plate, the behaviour is expected to be membrane-like in the process of kinetic energy absorption from the projectile. By contrast, for thick laminates, this behaviour is not observed. However, the projectile transfers some kinetic energy to the laminate. The hypothesis made to quantify this energy is to impose a contact condition. This condition considers that the laminate region in contact with the projectile moves with the same velocity as the projectile. The point at the leading edge of the compressive wave through the thickness direction has a velocity equal to zero. Between these two points, a profile of velocities must be assumed. In this case, a linear profile has been chosen. Only the material below the projected projectile diameter, which changes during the impact (15), is taken into account for this transfer.

Each differential of mass moves with a certain velocity changing with time. To account for and add the kinetic energy from all the differentials at any time, Eq. (25) is defined

$$\overline{E_{CL}}(\tau) = \frac{1}{2} \int_0^{\bar{m}(\tau)} \bar{v}(\bar{s}, \tau)^2 d\bar{m} \tag{25}$$

where $\bar{v}(\bar{s}, \tau)$ is the velocity as a function of a mute spatial variable $\bar{s}$ and time, $d\bar{m}$ is a differential of mass and $\bar{m}(\tau)$ is the mass affected by this phenomenon.

The differential of mass can be expressed as a function of the spatial variable

$$d\bar{m} = \frac{\pi}{4} \rho_l \bar{\phi}(\bar{x})^2 d\bar{s} \tag{26}$$

The velocity in Eq. (25) can be expressed as a function of the velocity of the projectile and the spatial variable assuming a linear profile of velocities

$$\bar{v}(\bar{s}, \tau) = \bar{v}(\tau) \left[1 - \frac{\bar{s}}{\overline{R_{xl}}(\tau)} \right] \tag{27}$$

Substituting (26) and (27) into (25), and integrating, the kinetic energy absorbed by the laminate can be determined.

3.2.5 Energy absorbed by shear plugging

Under high-velocity impact, thick laminates withstand high shear stresses whether they fail by this mechanism or not. The forces responsible for these stresses are generated around the projectile diameter in contact with the laminate. If these shear stresses are high enough and they surpass the maximum shear strength of the material in directions 13 and 23, the laminate can fail by shear plugging.

The differential energy absorbed by this mechanism may be obtained by multiplying the annular area by the maximum shear stress of the material in directions 13 and 23 and by the displacement of the projectile.

$$d\overline{E_{SP}} = \pi \bar{\phi}(\bar{x}) \Pi_E \Pi_{S_{SP}} d\bar{x} \tag{28}$$

where $\Pi_{S_{SP}}$ is the Π group related to the out-of-plane failure shear stress. If Eq. (28) is divided by $d\tau$, and then integrated, Eq. (29) is obtained

$$\overline{E_{SP}}(\tau) = \int_0^{\tau} \pi \bar{\phi}(\bar{x}) \Pi_E \Pi_{S_{SP}} \bar{v}(\tau) d\tau \tag{29}$$

3.2.6 Energy absorbed by delamination and matrix cracking

The energies absorbed by delamination and matrix cracking are related to the transverse wave and, thus, the bending of the laminate. The shape factor of the delaminated area, since this area is circular-shaped, has been demonstrated to be 1 (Alonso et al., 2018b). Therefore, the expressions to calculate matrix cracking and delamination are the following

$$\overline{E_{MC}}(\tau) = \pi \Pi_e \Pi_{E_{MT}} \overline{R_t}(\tau)^2 \tag{30}$$

$$\overline{E_{DL}}(\tau) = \pi \Pi_{G_{IICD}} \overline{R_t}(\tau)^2 \tag{31}$$

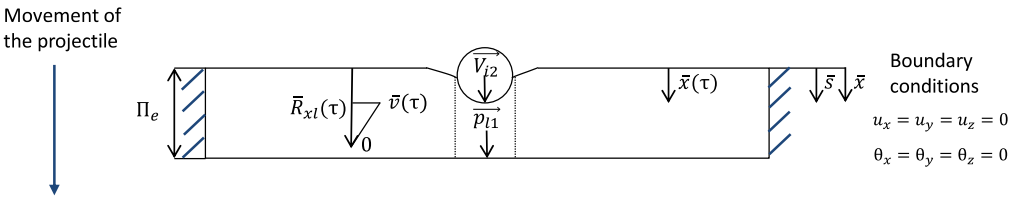

Fig. 5 Schema of the impact phenomenon at a precise instant of time of the second stage representing the variables and parameters involved

where $\Pi_{E_{MT}}$ and $\Pi_{G_{IICD}}$ are the Π groups related to the energy absorbed by matrix cracking per unit volume and to the critical dynamic-strain energy-release rate in mode II, respectively.

3.2.7 Energy balance and governing equation of the first stage

The mathematical treatment of this stage is formulated by means of an instantaneous energy balance. From a dimensional point of view, this balance can be formulated as in Eq. (32), which means that the initial kinetic energy of the projectile, E_0, is equal to the kinetic energy of the projectile at this moment, $E_p(t)$, plus the energy absorbed by the energy-absorption mechanisms until this moment, $E_{AB}(t)$

$$E_0 = E_p(t) + E_{AB}(t) \tag{32}$$

In its non-dimensional form, the balance adopts the following form

$$1 = \bar{v}(\tau)^2 + \frac{12}{\pi}\overline{E_{AB}}(\tau) \tag{33}$$

where $\overline{E_{AB}}(\tau)$ is defined as

$$\overline{E_{AB}}(\tau) = \overline{E_{C1}}(\tau) + \overline{E_{C2}}(\tau) + \overline{E_{TF}}(\tau) + \overline{E_{CL}}(\tau) + \\ + \overline{E_{SP}}(\tau) + \overline{E_{MC}}(\tau) + \overline{E_{DL}}(\tau) \tag{34}$$

Eq. (33) leads to the governing equation of the first stage. In order to achieve that, Eq. (33) must be derived with respect to non-dimensional time. Then, rearranging the terms, Eq. (35) is obtained with its initial conditions

$$\bar{a}(\tau) = \frac{\bar{g}\big(\tau, \bar{x}(\tau), \bar{v}(\tau)\big) - \bar{h}\big(\tau, \bar{v}(\tau)\big)\bar{v}(\tau) - \bar{f}\big(\tau, \bar{x}(\tau)\big)}{\frac{\pi}{6}\bar{v}(\tau) + \frac{\pi}{12}\Pi_{\rho_l} C_{v_{xl}} \bar{v}(\tau)\bar{\phi}(\bar{x})^2 \tau} - \\ - \frac{\frac{\pi}{24}\Pi_{\rho_l} C_{v_{xl}} \left[2\bar{v}(\tau)^3 \bar{\phi}(\bar{x}) \frac{d\bar{\phi}}{d\tau}\tau + \bar{v}(\tau)^2 \bar{\phi}(\bar{x})^2\right]}{\frac{\pi}{6}\bar{v}(\tau) + \frac{\pi}{12}\Pi_{\rho_l} C_{v_{xl}} \bar{v}(\tau)\bar{\phi}(\bar{x})^2 \tau} \tag{35}$$

$$\bar{x}(0) = 0$$

$$\bar{v}(0) = 1$$

To facilitate the handling of the terms, the various terms that appear in Eq. (35) are defined:

$$\bar{h}\big(\tau, \bar{v}(\tau)\big) = \frac{d}{d\tau}\left[\overline{E_{TF}}(\tau) + \overline{E_{SP}}(\tau) + \overline{E_{MC}}(\tau)\right] \tag{36}$$

$$\bar{g}\big(\tau, \bar{x}(\tau), \bar{v}(\tau)\big) = -\frac{d}{d\tau}\left[\overline{E_{C2}}(\tau) + \overline{E_{DL}}(\tau) +\right]\frac{1}{\bar{v}(\tau)} \tag{37}$$

$$\bar{f}\big(\tau, \bar{x}(\tau)\big) = \frac{d\overline{E_{C1}}(\tau)}{d\tau} \tag{38}$$

Note that this stage finishes when the stop condition given by Eq. (39) is met. At this moment, the velocity of the projectile is the initial velocity for the second stage.

$$\bar{x}(\tau) = \Pi_e \varepsilon_{rc} \tag{39}$$

3.3 Stage 2

At the end of the first stage, just before failure, the projectile moves with a certain linear momentum. Also, some kinetic energy has been transferred to a small part of the laminate. This part is the volume below the indented projected projectile diameter up to the radius of the compressive wave. Therefore, this part moves with a certain linear momentum too. Just after failure, the second stage, which is considered instantaneous nature, takes place. This stage is illustrated in Fig. 5.

In the second stage, a perfectly inelastic shock is assumed between the projectile and the plug formed. The latter is the cylinder with a diameter equal to that of the projectile and a height equal to the thickness. This last assumption is based on original observations and it was proposed by other authors (Potti and Sun 1997, Naik and Doshi 2005). After the shock, the two bodies move at the same velocity. At the transition moment between the first and the second stages, there are not exterior forces acting on the two bodies. Therefore, the momentum conservation principle can be applied

$$\overrightarrow{p_2} = \overrightarrow{p_3} \tag{40}$$

where $\overrightarrow{p_2}$ and $\overrightarrow{p_3}$ are the linear momentums at the beginning of the second and third stages respectively. Since the transfer of linear momentum takes place in one direction, Eq. (40) can be expressed as a scalar equation

$$p_{1l} + m_p v_{i2} = \big(m_p + m_l\big)v_{i3} \tag{41}$$

where p_{1l} is the accumulated linear momentum of the laminate at the end of the first stage, v_{i2} is the initial velocity at the second stage (which is the final velocity of

Table 5 Summary of the parameters and Π groups of the second stage.

Parameter	Nomenclature	Π group
Projectile diameter	ϕ_p	
Projectile density	ρ_p	
Initial velocity	v_{i2}	
Laminate thickness	e	$\Pi_e = \frac{e}{\phi_p}$
Compressive out-of-plane Young's modulus	E_c	$\Pi_{E_c} = \frac{E_c}{\rho_p v_{i2}^2}$
Projected diameter at the end of stage 1	ϕ_1	$\Pi_{\phi_1} = \frac{\phi_1}{\phi_p}$
Time at the end of stage 1	t_1	$\Pi_{t_1} = \frac{t_1 \rho_p}{v_{i1}}$
Laminate density	ρ_l	$\Pi_{\rho_l} = \frac{\rho_l}{\rho_p}$

the first one), m_p is the mass of the projectile, m_l is the mass of the plug formed and v_{i3} is the final velocity at the second stage (initial velocity at the third stage).

Although the only unknown parameter is v_{i3}, to maintain the non-dimensional formulation, the Vaschy-Buckingham Π Theorem is "artificially" used. Mass and length may be written in their non-dimensional form like in Eqs. (5) and (6). Time may be written as follows

$$[T] = \frac{\phi_p}{v_{i2}} \tag{42}$$

The problem depends on 8 fundamental parameters and, thus, 5 "artificial" Π groups can be formed. They are presented in Table 5.

The linear momentum stored in the plug when the second stage begins, p_{1l}, can be calculated by adding all the linear momentums from each differential of mass

$$p_{1l} = \int_0^{m_1} v(s) dm \tag{43}$$

where m_1 is the mass that has absorbed energy by transfer of kinetic energy in the first stage, $v(s)$ is the velocity which depends on a spatial variable and dm is a differential of mass. All these parameters are evaluated at the end of the first stage. Therefore, the differential of mass adopts the following form

$$dm = \frac{\pi}{4} \rho_l \phi_1^2 ds \tag{44}$$

The hypothesis of a linear profile of velocities was assumed for the energy absorbed by transfer of kinetic energy. So $v(s)$ may be written as in Eq. (45)

$$v(s) = v_{i2} \left[1 - \frac{s}{R_{xl}(t_1)} \right] \tag{45}$$

Substituting (44) and (45) into (43), and integrating, a new expression for the linear momentum of the laminate at the beginning of the second stage is obtained

$$p_{1l} = \frac{\pi}{8} \rho_l v_{xl} v_{i2} \phi_1^2 t_1 \tag{46}$$

The expressions for the mass of the projectile, as well as the mass of the laminate affected by the transfer of kinetic energy during the first stage, are defined as

$$m_p = \frac{\pi}{6} \phi_p^3 \rho_l \tag{47}$$

$$m_l = \frac{\pi}{4} \phi_p^2 e \rho_l \tag{48}$$

Substituting (46), (47) and (48) into (41), dividing the two sides of (41) by $\phi_p^3 \rho_l v_{i2}$, rearranging and treating v_{i3} as the variable to obtain, Eq. (49) is reached

$$\bar{v}_{i3} = \frac{3 \Pi_{\rho_l} \Pi_{t_1} \Pi_{\phi_1}{}^2 C_{v_{xl}} + 4}{6 \Pi_e \Pi_{\rho_l} + 4} \tag{49}$$

where $\bar{v}_{i3}$ is non-dimensional the initial velocity for the third stage.

3.4 Stage 3

In this last stage, the projectile moves in solidarity with the plug assuming as initial velocity the final velocity obtained from the second stage. The only energy-absorption mechanism that takes place in this stage is the friction between the projectile and the laminate. The friction force-displacement curve for each thickness was experimentally measured in this work.

The problem depends on three elemental magnitudes: mass and length may be written in their non-dimensional form like in Eqs. (5) and (6) and time as follows:

$$[T] = \frac{\phi_p}{v_{i3}} \tag{50}$$

where v_{i3} is the initial velocity at this stage.

The problem depends on 16 fundamental parameters which are presented in Table 6 with their corresponding Π groups. According to the Vaschy-Buckingham Π Theorem,

Table 6 Summary of the parameters and Π groups of the third stage representing the variables and parameters involved

Parameter	Nomenclature	Π group
Projectile diameter	ϕ_p	
Projectile density	ρ_p	
Initial velocity	v_{i3}	
Laminate thickness	e	$\Pi_e = \frac{e}{\phi_p}$
Laminate density	ρ_l	$\Pi_{\rho_l} = \frac{\rho_l}{\rho_p}$
Friction parameter 1	C_1	$\Pi_{C_1} = \frac{C_1}{\rho_p v_{i3}^2}$
Friction parameter 2	C_2	$\Pi_{C_2} = \frac{C_2}{\rho_p \phi_p v_{i3}^2}$
Friction parameter 3	C_3	$\Pi_{C_3} = \frac{C_3}{\rho_p \phi_p^2 v_{i3}^2}$
Friction parameter 4	C_4	$\Pi_{C_4} = \frac{C_4}{\rho_p v_{i3}^2}$
Friction parameter 5	C_5	$\Pi_{C_5} = \frac{C_5}{\rho_p \phi_p v_{i3}^2}$
Friction parameter 6	C_6	$\Pi_{C_6} = \frac{C_6}{\rho_p \phi_p^2 v_{i3}^2}$
Friction parameter 7	C_7	$\Pi_{C_7} = \frac{C_7}{\rho_p v_{i3}^2}$
Friction parameter 8	C_8	$\Pi_{C_8} = \frac{C_8}{\rho_p \phi_p v_{i3}^2}$
Friction parameter 9	C_9	$\Pi_{C_9} = \frac{C_9}{\rho_p \phi_p^2 v_{i3}^2}$
Length parameter 1	L_1	$\Pi_{L_1} = \frac{L_1}{\phi_p}$
Length parameter 2	L_2	$\Pi_{L_2} = \frac{L_2}{\phi_p}$

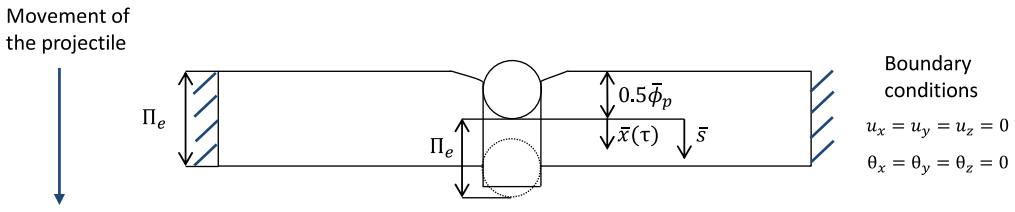

Fig. 6 Schema of the impact phenomenon at a generic instant of time in the third stage

the number of parameters on which the problem depends has been reduced from 16 to 13.

Π_{C_i} for $i = 1$ to 9 represents the coefficients of the experimental friction force-displacement curve in their non-dimensional form and they were identified in the experimental section. Π_{L_i} for $i = 1, 2$ represents the non-dimensional displacements which bracket the intervals of the experimental friction force-displacement curve because it is defined by pieces.

A generic time during this stage with the variables involved is illustrated in Fig. 6.

The combined amount of energy lost by the projectile and plug through their path across the laminate may be expressed at any time by Eq. (51)

$$\Delta \mathrm{E_f}(t) = \frac{1}{2}(m_p + m_l)(v_{i3}^2 - v(t)^2) \tag{51}$$

In its non-dimensional form, with m_p and m_l defined in Eqs. (47) and (48) respectively, Eq. (51) turns into Eq. (52)

$$\Delta\overline{E_f}(\tau) = \frac{\pi}{4}\left(\frac{1}{3} + \frac{1}{2}\Pi_e\Pi_{\rho_l}\right)(1 - v(t)^2) \tag{52}$$

This lost energy is the energy below the experimental friction force-displacement curve presented in the experimental section. The hole for the friction tests was slightly smaller than the hole for the projectile. For this reason, the ranges of the curve are 9 mm and 12 mm. As can be seen in Fig. 6, half of the projectile is approximately indented in the starting position, and the final position takes place when the other half of the projectile has completely gone through all the plate. An additional hypothesis needs to be assumed to use this curve. This is that although the failure during stage 1 does not exactly occur with an indentation equal to the radius, it is approximately equal to it. In this way, from the beginning of stage 3 we are at the position where the friction curve starts. With a simple calculation using Eqs. (39) and (15), the indented diameter at the moment of failure can be determined for 9 mm and 12 mm specimens, which are ϕ_{f9} = 6.58 mm and ϕ_{f12} = 7.14 mm mm respectively, not so far from the 7.5 mm given by the projectile diameter.

Making the last assumption, the loss of energy can also be calculated from the beginning of the third stage by means of the friction force-displacement curve (53). An additional consideration is that the reference system in this last stage is moved so that the initial position of the third stage is zero

$$\Delta\overline{E_f}(\tau) = \int_0^{\bar{x}(\tau)} \bar{f}(\bar{s})d\bar{s} \tag{53}$$

where $\bar{f}(\bar{s})$ is the friction force-displacement curve as a function of a mute spatial variable $\bar{s}$

$$\bar{f}(\bar{s}) = \begin{cases} \Pi_{C_1}\bar{s}^2 + \Pi_{C_2}\bar{s} + \Pi_{C_3}, & if \;\; 0 < \bar{s} \le \Pi_{L_1} \\ \Pi_{C_4}\bar{s}^2 + \Pi_{C_5}\bar{s} + \Pi_{C_6}, & if \;\; \Pi_{L_1} < \bar{s} \le \Pi_{L_2} \\ \Pi_{C_7}\bar{s}^2 + \Pi_{C_8}\bar{s} + \Pi_{C_9}, & if \;\; \Pi_{L_2} < \bar{s} \le \Pi_e \end{cases} \tag{54}$$

Combining Eqs. (52) and (53) and deriving with respect to non-dimensional time, Eq. (55) is obtained

$$\frac{\pi}{2}\left(\frac{1}{3} + \frac{1}{2}\Pi_e\Pi_{\rho_l}\right)a(t) = -\bar{f}\left(\bar{x}(\tau)\right) \tag{55}$$

Stating the initial conditions, a second-order differential equation is obtained

$$\bar{a}(\tau) = \frac{-\bar{f}\left(\bar{x}(\tau)\right)}{\frac{\pi}{2}\left(\frac{1}{3} + \frac{1}{2}\Pi_e\Pi_{\rho_l}\right)} \tag{56}$$

$$\bar{x}(0) = 0$$

$$\bar{v}(0) = 1$$

This last stage finishes when the condition given by Eq. (56) is fulfilled, which is the moment when the projectile is no longer in contact with the plate as can be seen in Fig. 6:

$$\bar{x}(\tau) = \Pi_e \tag{57}$$

4. Numerical modelling and correspondence with the theoretical model

The 3D finite element model developed by Alonso *et al*. (2020) has been used in order to provide further validity to the theoretical model presented above. The constitutive equations and failure criteria are introduced to allow for the comparison between both theoretical and FE models. Further explanation of this model is given in Alonso *et al*. (2020). A continuum damage mechanics approach is used where the failure criteria are formulated in such a way that a clear correlation with the energy-absorption mechanisms described in the theoretical model can be found. Considering that the material response is linear-elastic until the onset of damage, the constitutive equation may be written in Mandel's notation as

$$\begin{bmatrix} \varepsilon_{11} \\ \varepsilon_{22} \\ \varepsilon_{33} \\ \gamma_{12} \\ \gamma_{23} \\ \gamma_{13} \end{bmatrix} = \begin{bmatrix} \frac{1}{E_{11}(1-d_1)} & 0 & 0 & & & \\ 0 & \frac{1}{E_{22}(1-d_2)} & 0 & & 0_{3x3} & \\ 0 & 0 & \frac{1}{E_{33}(1-d_3)} & & & \\ & & & \frac{1}{G_{12}(1-d_4)} & 0 & 0 \\ & 0_{3x3} & & 0 & \frac{1}{G_{23}(1-d_5)} & 0 \\ & & & 0 & 0 & \frac{1}{G_{13}(1-d_6)} \end{bmatrix} \begin{bmatrix} \sigma_{11} \\ \sigma_{22} \\ \sigma_{33} \\ \sigma_{12} \\ \sigma_{23} \\ \sigma_{13} \end{bmatrix} \tag{58}$$

where ε_{ii} and γ_{ij}, with $i = \{1,2,3\}$ and $j = \{1,2,3\}$, are the components of the strain tensor; σ_{ij}, with $i = \{1,2,3\}$ and $j = \{1,2,3\}$ are the components of the stress tensor; E_{ii}, ν_{ij} and G_{ij} are the Young's moduli, Poisson's ratios and shear moduli, with $i = \{1,2,3\}$ and $= \{1,2,3\}$; and d_i are damage parameters associated with different failure mechanisms. The fracture toughness at each direction is the responsible for controlling the damage variables evolution once they have been activated.

Since the model is formulated in 3D, the failure criteria can be classified in in-plane and out-of-plane. The following in-plane criteria were used for the onset of damage.

The fibre failure criterion is associated with tensile failure of fibres in the theoretical model. When Eqs. (59) or (60) are met, the damage variables related to the failure of fibres in tension or compression are activated. This criterion for woven laminates was firstly used by Chang and Chang (1987)

$$\left(\frac{\sigma_{11}}{X_{11i}}\right)^2 + \left(\frac{\sigma_{12}}{S_{12}}\right)^2 + \left(\frac{\sigma_{13}}{S_{13}}\right)^2 = 1 \tag{59}$$

$$\left(\frac{\sigma_{22}}{X_{22i}}\right)^2 + \left(\frac{\sigma_{12}}{S_{12}}\right)^2 + \left(\frac{\sigma_{13}}{S_{13}}\right)^2 = 1 \tag{60}$$

where X_{lli} are the normal failure stresses associated with $l = \{1,2,3\}$; S_{12}, S_{13}, S_{23} are the shear failure stresses associated with directions 12, 13 and 23 and $i = \{t,c\}$ accounts for tension and compression.

The matrix cracking failure criterion is associated with matrix cracking in the theoretical model. This failure criterion is based on that proposed by Hashin (1980), in which a failure due to in-plane shear tension is assumed

$$\left(\frac{\sigma_{12}}{S_{12s}}\right)^2 = 1 \tag{61}$$

where S_{12s}, S_{13s}, S_{23s} are the matrix shear failure stresses associated to directions 12, 13 and 23. This approach was also used in the model proposed by Xiao *et al*. (2007).

Regarding to the out-of-plane failure criteria, they can be classified in the following groups:

The criterion involving the out-of-plane shear stresses is associated with shear plugging. This effect gains importance when increasing the thickness of the laminate

$$\left(\frac{\sigma_{13}}{S_{13s}}\right)^2 + \left(\frac{\sigma_{23}}{S_{23s}}\right)^2 = 1 \tag{62}$$

The crush failure criterion is associated with the compression in both regions along the thickness direction

$$\left(\frac{\sigma_{33}}{X_{33}}\right)^2 = 1 \tag{63}$$

In order to account for the delamination between plies, which is associated with delamination in the theoretical model, an interlaminar damage model is used. It is defined by the classic cohesive zone method, which is governed by a traction-separation law (Turon *et al*. 2007). All the details about the interlaminar damage model and, in general, about the finite element model can be found in Alonso *et al*. (2020).

Note that friction is associated with friction in the theoretical model and the kinetic energy of the elements is associated with the sum of the kinetic energy transferred to the laminate during the first stage plus the instantaneous transfer of kinetic energy in the second stage.

The experimental procedure to carry out the impact test is described next. First the projectile was placed in a pressure chamber and a high-resolution camera was located parallel to the laminate which is embedded by its borders in a frame of steel (150x150 [mm^2]). Then, the projectile was propelled with Helium gas against the laminate and the camera recorded the whole event allowing for the determination of the residual velocity with an image correlation software afterwards. Further details are described by Alonso *et al*. (2018a).

The finite element simulations were carried out with the same set-up as in the experimental tests with thicknesses of 9 and 12 mm. Lagrangian 3D reduced integration elements (Abaqus C3D8R) were used to simulate the plies. Cohesive elements (Abaqus COH3D8) were also used to simulate delamination, with a thickness of 0.001 mm between plies. The boundary conditions applied are: the laminate edges nodes fixed and initial velocity given to the projectile. The mesh is divided in two regions, a finer mesh in the impact zone and coarser as the distance to the center increases. The mesh characteristics are listed in Table 7. The damage variables go from 0 (bulk material, i.e., non-damaged) to 1 (complete degradation).

Table 7 Type and number of elements used in the definition of the numerical models for the four thicknesses

Thickness [mm]	C3D8R	COH3DR	Total
9	1342260	417592	1759852
12	2012940	637431	2650371

Further details of the finite element model definition can be found in Alonso *et al*. (2020).

5. Results and discussion

The aim of this section is to present the results obtained by the theoretical model and their comparison with experimental and computational tests. First, the model is validated against experimental data from the literature by means of the ballistic perforation tests (Alonso *et al*. 2018a), (Buitrago *et al*. 2010). The most important output from the theoretical model is the ballistic limit and residual velocity under impact conditions. To further analyse the predictive capability of the model, different parameters and hypotheses are studied with the aid of the finite element model.

5.1 Validation of the theoretical model

Fig. 7 shows a comparison between the experimental results for high-velocity impact on E/glass fibre/polyester plates obtained by Alonso *et al*. (2018a) for 9 mm and by Buitrago *et al*. (2010) for 12 mm thickness and the theoretical and finite element predictions.

A good agreement was found between the theoretical model and the experimental results in terms of the ballistic limit and the residual velocities. The highest error made by the theoretical model was below 2 % in terms of the ballistic limit and a good fitting is observed for the residual velocities. The finite element model also provided a good fit in terms of the ballistic limit up to a certain velocity. However, from an approximate velocity of 600 m.s^{-1}, the predictions diverged with respect to the experimental data. From this point, the finite element model predicts lower residual velocities than those found experimentally, implying an overestimation of the energy-absorption predicted by the model. Since this behaviour always takes place from a very high-velocity, it may be explained as an effect of temperature increment during the perforation process due to dissipative contributions. Many authors such as Hufenbach *et al*. (2011); Bai *et al*. (2008); Ou *et al*. (2016), Shaoquan *et al*. (2017) have explained the influence of temperature on the mechanical properties of composite materials. When such high velocities are reached, high temperatures arise within the laminate and they can provoke the softening phenomenon. This effect mainly occurs within the matrix of the composite. In this regard, polymer matrices usually present high sensitivity of mechanical properties with temperature (Garcia-Gonzalez *et al*. 2017). As a consequence of the so-called softening phenomenon (caused by thermal softening), these properties normally

decrease with temperature, reducing the stiffness of the material and thus its capacity to absorb energy. Furthermore, with high strain rate processes, the inelastic energy during deformation and/or fracture dissipates much faster than heat conduction leading to adiabatic conditions and important temperature increase. In addition, matrix heat conductivity is low, so for a short time (high-velocity impact) energy dissipation is nearly an adiabatic process with high temperature increase (Garcia-Gonzalez *et al*. 2017).

In Table 8, the results of the ballistic limits of both models are compared with the experimental data, showing maximum differences below 1% in all cases.

5.2. Analysis of the Π groups dependences

The effects of the most important Π groups were analysed to evaluate the physical consistency of the model. Thick enough laminates present compression and shear plugging as the main energy-absorption mechanisms (Alonso *et al*. 2018a). Therefore, to further study this point, we carried out a parametric study of the parameters which control these mechanisms.

5.2.1 Analysis of the out-of-plane compressive Young's modulus Π group

The Π group involving the compressive Young's modulus through the thickness direction, Π_{E_c}, is a dominant parameter in the theoretical model for thick laminates since it plays a major role in the energy absorbed by compression: Eq. (14), Eq. (19) and in the compressive wave along the through-thickness direction: Eq. (10). The results given by the theoretical model when varying the through-thickness Young's modulus are presented in Fig. 8.

From the curves shown in Fig. 8, it can be inferred that the higher the compressive through-thickness Young's modulus, the higher the ballistic limit.

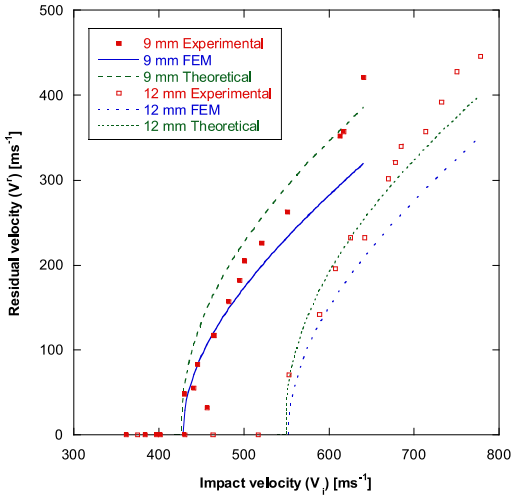

Fig. 7 Comparison between the ballistic results provided by the theoretical and FEM models with experimental data

Table 8 Experimental, theoretical and numerical results of the ballistic limit

Ballistic limit [m.s^{-1}]			
Thickness [mm]	**Experimental**	**Theoretical**	**Numerical**
9	428	428	430
12	550	551	553

Table 9 Total energies absorbed by each energy-absorption mechanism for 9 mm thick specimens with different compressive through-thickness Young's moduli for an impact velocity of 850 m.s^{-1}

E_c[GPa]	E_{C1}[J]	E_{C2}[J]	E_{TF}[J]	E_{CL}[J]	E_{SP}[J]	E_{DL}[J]	E_{MC}[J]
1.35	2.10	0	4.61	13.95	51.35	0.02	0.05
3.375	8.35	0	4.62	21.60	51.35	0.02	0.05
6.75	23.80	0	4.64	29.45	51.35	0.02	0.05
13.5	68.61	0	4.68	38.03	51.35	0.02	0.05
33.75	300.3	0	4.87	33.68	51.35	0.02	0.07

At a certain velocity, all the curves tend to a common curve. This convergence is obtained for 9 mm thick or thicker specimens, as can be observed when comparing Figs. 8 and 8b. In order to see the influence of Π_{E_c}, the energy-absorption mechanisms are compared for a 9 mm thick specimen for a velocity of 850 m.s^{-1}. These results are shown in Table 9.

The energies affected by a change in E_c are quantitatively shown in Table 9: compression in region 1, which is directly proportional to E_c, Eq. (14); the transfer of kinetic energy to the laminate, Eq. (25). The latter increases as a consequence of the through-thickness wave velocity, Eq. (10). This wave velocity increases with E_c and, thus, the energy transferred to the laminate is higher. As these two energy-absorption mechanisms increase while the others remain constant, the ballistic limit increases with E_c.

Another remarkable observation is that the energy absorbed by compression in region 2 is zero for all the cases. This can be explained by the high impact velocity that does not allow the transverse wave to reach the indented projectile diameter before the second stage starts.

5.2.2 Analysis of the out-of-plane failure shear stress Π group

Out-of-plane effects gain importance in the impact phenomenon as the thickness increases. Shear plugging is controlled by out-of-plane shear stresses, which reach quite high values for high thicknesses. In fact, this energy-absorption mechanism is one of the most important in thick laminate as demonstrated by Alonso *et al*. (2018a). The parameter $\Pi_{S_{SP}}$ directly affects the energy absorbed by shear plugging because they are proportional, Eq. (29). The results provided by the theoretical model for thick laminates varying the out-of-plane failure shear stress are shown in Fig. 10.

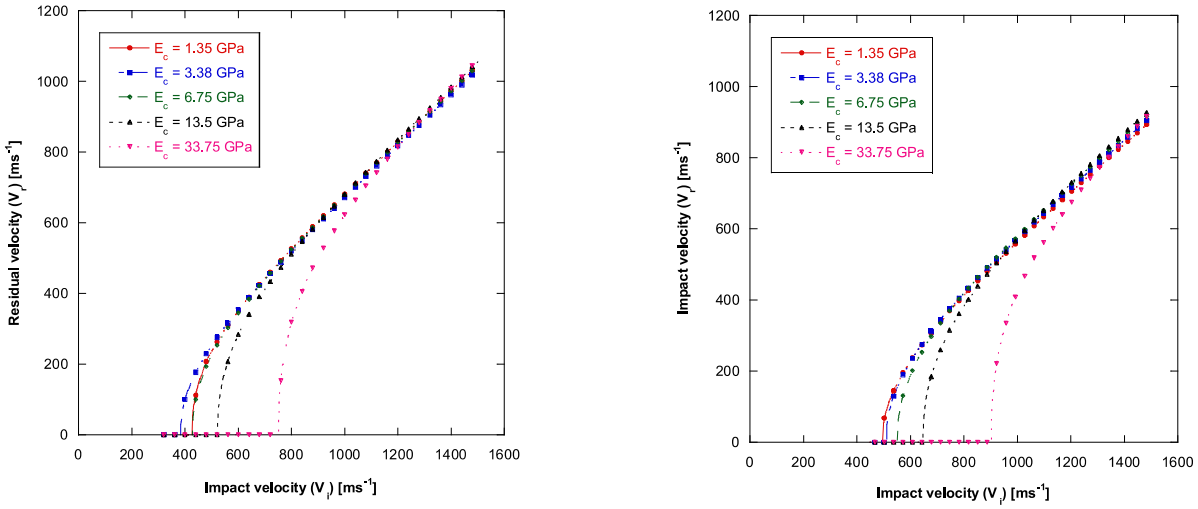

(a) (b)

Fig. 8 Impact velocity (V_i) vs residual velocity (V_r) for different compressive through-thickness Young's moduli for laminates of (a) 9 mm (b) 12 mm

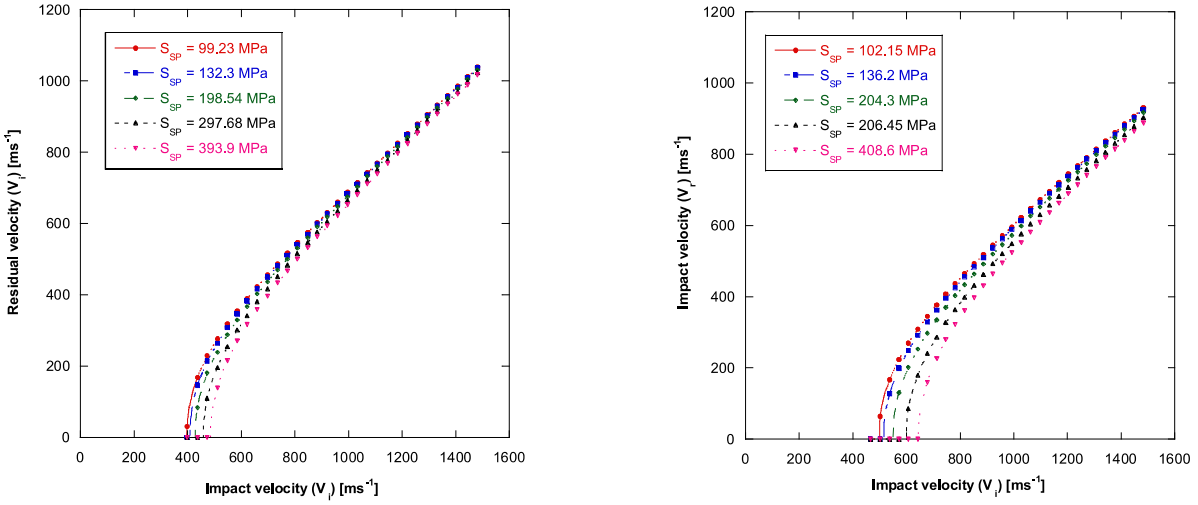

(a) (b)

Fig. 9 Impact velocity (V_i) vs residual velocity (V_r) for different out-of-plane failure shear stresses for (a) 9 mm (b) 12 mm thick laminates

Table 10 Total energies absorbed by each energy-absorption mechanism for 12 mm thick specimens with different out-of-plane failure shear stresses for an impact velocity of 650 m.s^{-1}

S_{SP}[MPa]	E_{C1}[J]	E_{C2}[J]	E_{TF}[J]	E_{CL}[J]	E_{SP}[J]	E_{DL}[J]	E_{MC}[J]
102.15	51.64	0	10.35	27.61	52.49	0.06	0.24
136.2	52.37	0	10.41	25.91	69.99	0.06	0.24
204.3	54.01	0	10.54	22.39	105.0	0.07	0.26
306.45	57.09	0	10.76	16.77	157.5	0.07	0.29
408.6	61.52	0	11.02	10.52	210.0	0.08	0.34

Figs. 9(a) and 9(b) reveal that the higher the out-of-plane failure shear stress, the higher the ballistic limit. The same tendency, as in the other parametric studies, is observed: all the curves collapse into one at very high velocities.

The energy-absorption mechanisms were analysed by means of the variation of S_{SP} for an impact velocity of 650 m.s^{-1}. These results are shown in Table 10, which shows that S_{SP} affects all the energy-absorption mechanisms. However, the most affected mechanism is shear plugging. In view of Eq. (29), an increase in S_{SP} provokes an increase in the energy absorbed by this mechanism and, consequently, the ballistic limit.

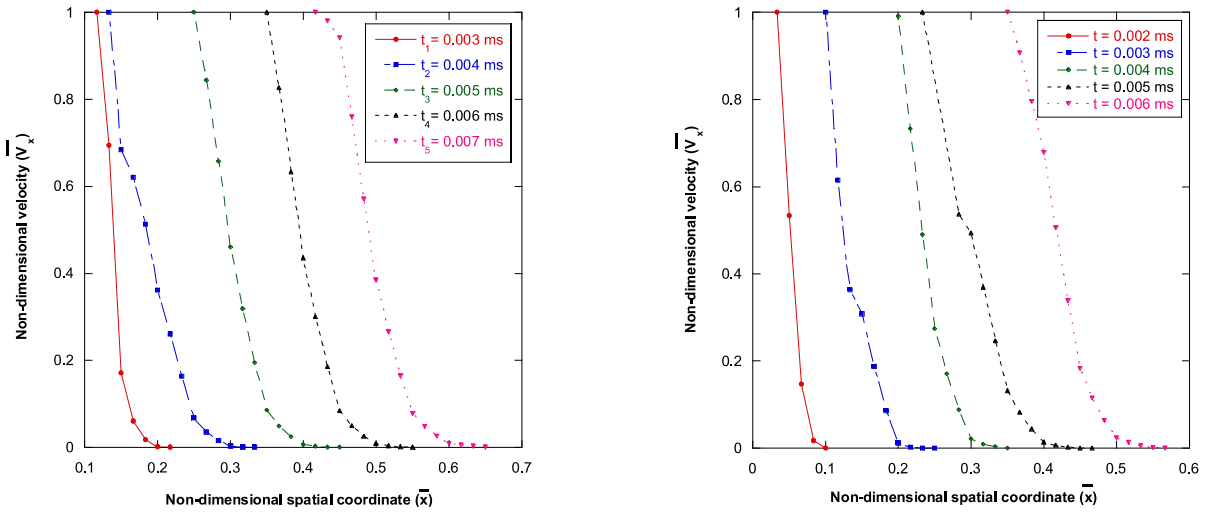

Fig. 10 Non-dimensional velocity of a path of nodes along the thickness ($\bar{V}_x$) vs non-dimensional position along the thickness ($\bar{x}$) for different instants of time for a 9 mm thick specimen for impact velocities of (a) 465 m.s^{-1} (b) 501 m.s^{-}

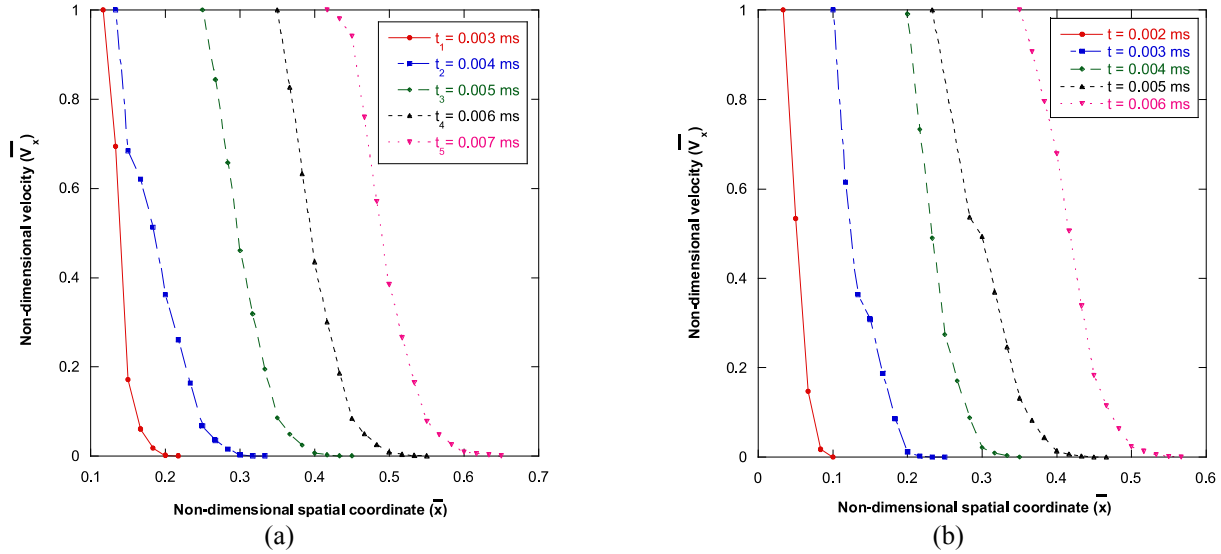

Fig. 11 Non-dimensional velocity of a path of nodes along the thickness ($\bar{V}_x$) vs non-dimensional position along the thickness ($\bar{x}$) for different instants of time for a 12 mm thick specimen for impact velocities of (a) 553 m.s^{-1} (b) 625 m.s^{-1}

Note that the energy absorbed by compression in region 2 is zero for all the cases. This can be explained by the high impact velocity for both cases and the faster growth of the indented projectile diameter with respect to the transverse wave, as in the case of Π_{E_c}.

5.3 Validation of the theoretical model hypotheses: Profile of velocities across the thickness direction

One of the hypotheses assumed in the theoretical model for thick laminates is the existence of a profile of velocities across the thickness direction. This profile was supposed to be linear between the contact point and the distance travelled by the compressive through-thickness wave, Eq. (27). In order to check this assumption, the following procedure was followed in the finite element model. First, a path of nodes is created along the thickness direction. This path goes from the upper layer to the bottom layer. The profile of velocities changes in each increment of time and also some of the elements belonging to the path are deleted at some point as result of the failure model implementation. These aspects must be taken into account to obtain reliable results. In this way, the velocity versus position can be known for each increment.

In Figs. 10 and 11, the first point represented for each time increment is slightly ahead of the most advanced part of the projectile to avoid problems that can introduce false data (such as deletion of elements). The last point is that

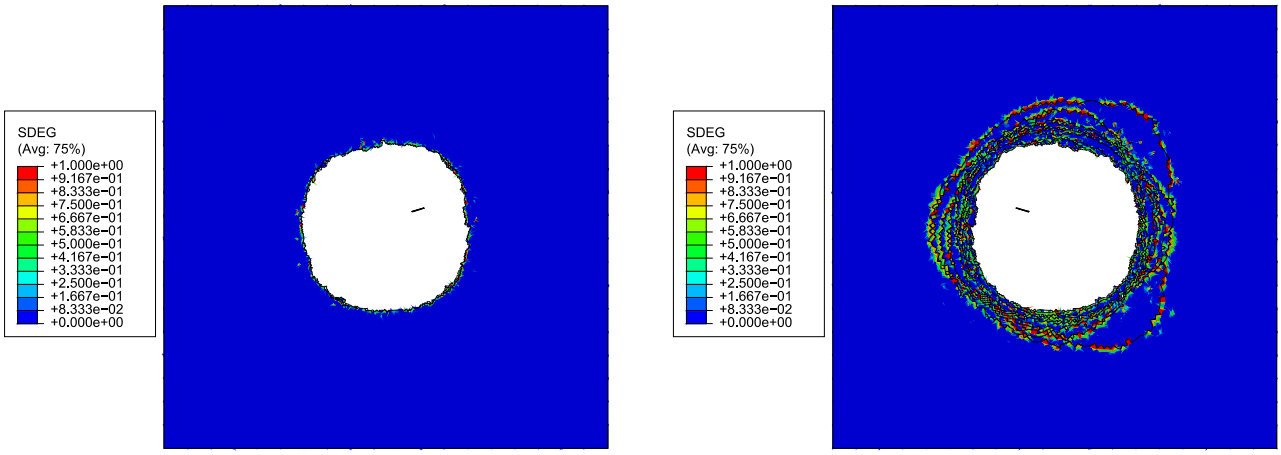

(a) (b)

Fig. 12 Numerical predicted damage on the (a) front and (b) rear faces for a 9 mm thick specimen impacted at 430 \m.s^{-1} (slightly above the ballistic limit)

reached by the compressive wave through the thickness direction at each increment. The velocity of each element in the thickness direction, v_z, is obtained for each increment of time. The velocity is non-dimensionalized with respect to the maximum velocity at each time increment, which corresponds to the velocity in the closest node to the projectile. The spatial coordinates, z, are represented in the undeformed configuration and they are non-dimensionalized with respect to the thickness.

Four cases were studied corresponding to 9 mm and 12 mm thick specimens at two different impact velocities, approximately the ballistic limit and slightly above it. In Fig. 10, the velocity along the path versus the thickness coordinate is represented for 9 mm thick specimens for velocities of 465 m.s^{-1} and 501 m.s^{-1} (Figs. 10(a) and 10(b), respectively). The same features are represented in Fig. 11 but for 12 mm thick specimens for velocities of 553 m.s^{-1} and 625 m.s^{-1} (Figs. 11(a) and 11(b), respectively).

The profile of velocities is represented until the transition from the first stage to the second stage occurs. Therefore, in Figs. 10 and 11 the final time corresponds with the time at which Eq. (39) is satisfied (Fig. 4).

The shape of the velocities profiles along the thickness is rather similar for all the cases studied. Therefore, from now on, the upcoming discussion and conclusions refer to all cases. From Figs. 10 and 11, it can be inferred that the velocity always decreases for points farther away from the impact point. In this regard, the curve moves to the right when time increases because the projectile advances and, then, the compressive wave, while the shape remains similar. Regarding the shape of the velocities profiles, it resembles a straight line with approximately the same slope for all the cases. In view of these results, the hypothesis of a linear gradient of velocities from the point in contact between the two bodies and the distance travelled by the through-thickness compressive wave seems reasonable.

5.4 Analysis of material damage after impact

The continuum damage of the impacted samples is studied by means of surface delamination. The FEM model can be used to qualitatively measure the shape and distribution of damage surfaces. All the simulated cases present a general pattern in damage distribution after impact. Representative results are shown in Figs. 12(a) and 12(b), where the prediction of damage on both the front and rear faces for undeformed configuration and they are non-dimensionalized with respect to the thickness.

Four cases were studied corresponding to 9 mm and 12 mm thick specimens at two different impact velocities, approximately the ballistic limit and slightly above it. In Fig. 10, the velocity along the path versus the thickness coordinate is represented for 9 mm thick specimens for velocities of 465 m.s^{-1} and 501 m.s^{-1} (Figs. 10(a) and 10(b), respectively). The same features are represented in Fig. 11 but for 12 mm thick specimens for velocities of 553 m.s^{-1} and 625 m.s^{-1} (Figs. 11(a) and 11(b), respectively).

The profile of velocities is represented until the transition from the first stage to the second stage occurs. Therefore, in Figs. 10 and 11 the final time corresponds with the time at which Eq. (39) is satisfied (Fig. 4).

The shape of the velocities profiles along the thickness is rather similar for all the cases studied. Therefore, from now on, the upcoming discussion and conclusions refer to all cases. From Figs. 10 and 11, it can be inferred that the velocity always decreases for points farther away from the impact point. In this regard, the curve moves to the right when time increases because the projectile advances and, then, the compressive wave, while the shape remains similar. Regarding the shape of the velocities profiles, it resembles a straight line with approximately the same slope for all the cases. In view of these results, the hypothesis of a linear gradient of velocities from the point in contact between the two bodies and the distance travelled by the through-thickness compressive wave seems reasonable.

5.4 Analysis of material damage after impact

The continuum damage of the impacted samples is studied by means of surface delamination. The FEM model

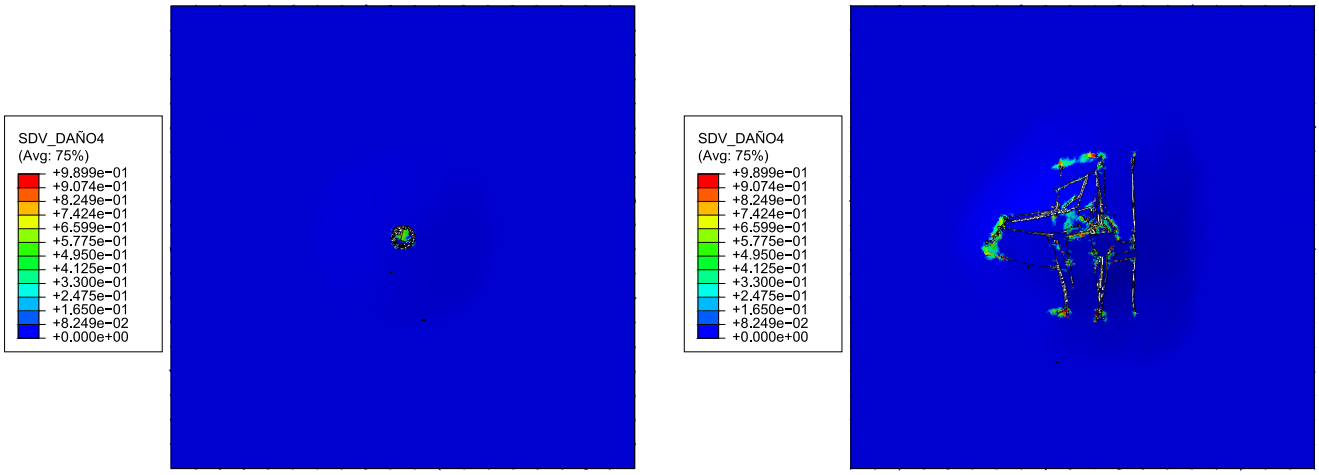

(a) (b)

Fig. 13 Representation of the damage variable d_4, which accounts for matrix cracking, on the (a) front and (b) rear faces for a 9 mm thick specimen impacted at 430 m.s^{-1} (slightly above the ballistic limit)

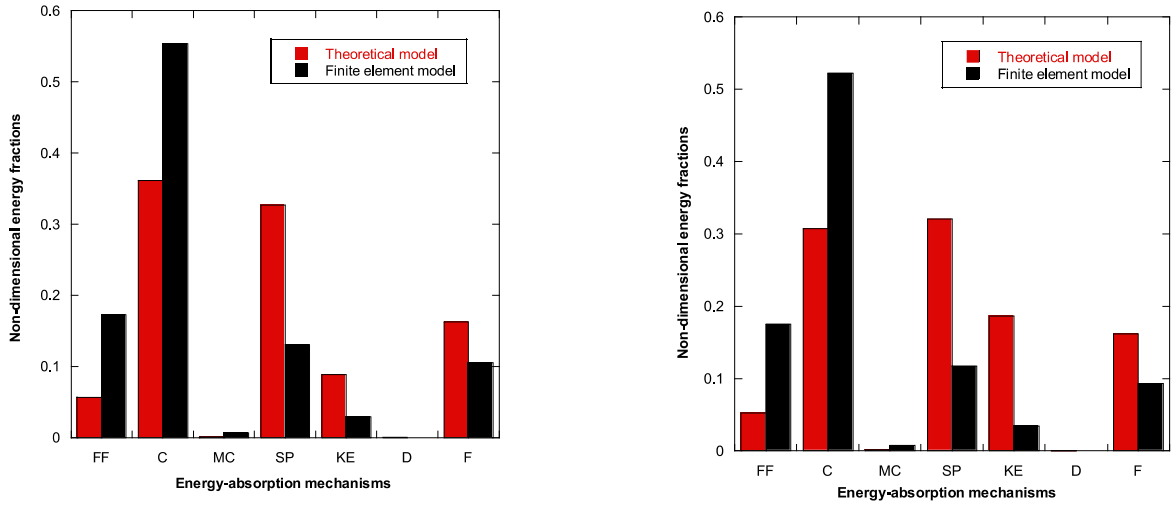

(a) (b)

Fig. 14 Theoretical and numerical non-dimensional energy fractions from left to right: Failure of fibres (FF), compression (C), matrix cracking (MC), shear plugging (SP), transfer of kinetic energy (KE), delamination (D) and friction (F) for a 9 mm thick specimen subjected to impact velocities of (a) 430 m.s^{-1} (b) 465 m.s^{-1}

can be used to qualitatively measure the shape and distribution of damage surfaces. All the simulated cases present a general pattern in damage distribution after impact. Representative results are shown in Figs. 12(a) and 12(b), where the prediction of damage on both the front and rear faces for
a 9 mm thick specimen impacted at 430 m.s^{-1} are presented. Note that these results represent a critical impact velocity close above the ballistic limit, which is of great interest since it is considered the most important condition for the design of these structures.

Figs. 12(a) and 12(b) capture the circular shape of the damaged area. This shape is experimentally confirmed in previous studies (Alonso *et al*. 2018b, Gil-Alba *et al*. 2019).

Furthermore, the damaged area on the rear face (Fig. 12(b)) is larger than the one in the front face (Fig. 12(a)). This matches the trends observed experimentally, showing a good predictive capability of the FEM model.

Figs. 13(a) and 13(b) show the damage variable d_4, which accounts for matrix cracking, on the front and rear faces for a 9 mm thick specimen impacted at 430 m.s^{-1}. These distributions can be related to the damage surfaces (delamination) as shown in Fig. 12.

From Fig. 13(a) it can be inferred that there is not remarkable permanent damage due to matrix cracking on the front face after impact since in the first instants the projectile easily penetrates because the momentum transfer to the laminate is negligible and only a small local zone is

affected. Nevertheless, Fig. 13(b) shows that the damage related to the parameter d_4 is more extended, reaching the furthest parts of the fracture surface, since this part of the laminate had more time to move and bend leading to a larger delaminated area and matrix cracking.

5.5 Analysis of energy-absorption mechanisms

Energy-absorption capacity and failure mechanisms are key factors in the design of structures and mechanical components (Martínez-Hergueta *et al*. 2015, Hongyong *et al*. 2017, Zhu *et al*. 2018). One of the principal advantages of the finite element model is that the failure criteria are defined with certain equivalences to the theoretical model. The intention was to be able to associate a group of failure criteria in the finite element model to a failure mode or energy-absorption mechanism in the theoretical model. In this section, the amount of energy absorbed by each mechanism is analysed. The procedure to obtain the energies follows the methodology presented by Alonso *et al*. (2020).

The equivalences between the energy-absorption mechanisms of the theoretical and the finite element models can be consulted in the numerical modelling section. The comparison carried out in this section aims at assessing the general trends of the energies absorbed in both models and comparing them.

The energy-based study was carried out at velocities near the ballistic limit for one of the thicknesses. The ballistic limit is a critical feature to ensure safety and structural integrity. Therefore, we analyse the following velocities: 430 m.s^{-1} and 465 m.s^{-1} for 9 mm. The comparison of the absorbed energies for 9 mm thick specimens is shown in Fig. 14.

For a velocity slightly below the ballistic limit for the 9 mm thickness specimen, Fig. 14(a) shows that the major energy-absorption mechanism for both models is compression. This mechanism is followed by shear plugging in the theoretical model. The remaining energy-absorption mechanisms are minor. For a velocity slightly above the ballistic limit, Fig. 14(b) shows that compression is still the most important energy-absorption mechanism in the finite element model. However, this role is shared between compression and shear plugging in the theoretical model. Matrix cracking and delamination play a minor role both models (see Figs. 14(a) and 14(b)). It is worth to highlight that both models suggest the out-of-plane damage mechanisms (compression and shear plugging) to play the major role in thick laminates. The predictions from both models, by means of energy-absorption mechanisms, are consistent showing the same tendencies in terms of relative contribution.

Overall, both the theoretical and the finite element models provide consistent results in terms of the relative roles of the energy-absorption mechanisms (see the trends shown in Fig. 15). In this regard, Fig. 15 shows a comparison by means of energy-absorption mechanisms grouped into in-plane and out-of-plane components for the loading cases presented in Fig. 14(b) and a 12 mm thick specimen impacted at 517 m.s^{-1}. Note that both models

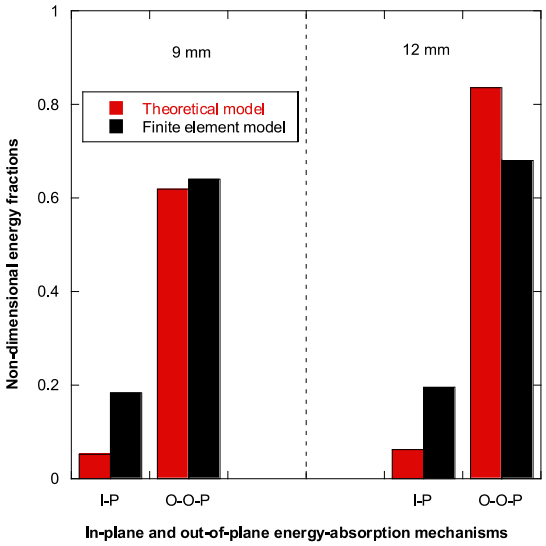

Fig. 15 Comparison between out-of-plane (O-P) and in-plane (I-P) energy-absorption mechanisms for: a 9 mm thick specimen impacted at 465 m.s^{-1} and a 12 mm thick specimen impacted at 517 m.s^{-1}

predict that the out-of-plane predominate over in-plane energy-absorption mechanisms. These observations are consistent with previous works that highlighted the fact that the out-of-plane energy-absorption mechanisms become more significant with increasing thickness (Alonso *et al*. 2020).

6. Conclusions

The work performed in this paper is focused on the study of high-velocity impact on thick woven GFRP plates. We develop a new non-dimensional energy-based theoretical model. This theoretical model for thick laminates considers different energy-absorption mechanisms and splits the impact phenomenon into three stages. The governing equation of the first stage is a non-linear second-order differential equation that can be solved by numerical integration. The second stage is instantaneous; the last stage is also governed by a second-order differential equation. This model is formulated with new phenomenological (but physically motivated) hypotheses to provide a more reliable approach to the impact problem.

The results by means of ballistic limits and residual velocities show good agreement between the theoretical model and the experimental results. However, the finite element model does not provide accurate results for very high velocities although it accurately predicts the ballistic limit. Once the models were validated against experimental results, two representative Π groups were studied to see the physical consistency of the theoretical model. Since the importance of the energy-absorption mechanisms changes for thick laminates and the out-of-plane mechanisms gain importance, the Π groups analysed were Π_{E_c} and $\Pi_{S_{SP}}$. It was observed that the higher these parameters, the higher

the ballistic limit, explained by an increase of the energy absorbed by compression and shear plugging.

Furthermore, some of the hypotheses assumed in the theoretical model were analysed with the help of the finite element model. The profile of velocities through the thickness direction was assumed linear in the theoretical model. The results show that the linear approximation fits the profile obtained with the finite element model well for the two thicknesses analysed. In addition, the qualitative shape of damage in the specimens after impact is the same as that experimentally observed. Moreover, the energy-absorption mechanisms provided by the theoretical and finite element models were compared, leading to an interesting discussion. The out-of-plane energy-absorption mechanisms (compression and shear plugging) are those that control the perforation process in the theoretical and finite element models. In addition, the importance of out-of-plane effects increases with thickness. Friction is also slightly more important for the thickest specimens and the theoretical and finite element models follow the same trend. The other energy-absorption mechanisms are of minor importance with the exception of the transfer of kinetic energy, that increases significantly in the theoretical model when perforation takes place.

Acknowledgments

L. Alonso, S.K.García Castillo and C.Navarro are indebted to the project 'Acción Estratégica en Materiales Compuestos y Análisis Numérico simplificado de Estructuras y protecciones ligeras sometidas a impacto balístico' (2010/00309/002) of the University Carlos III of Madrid for the financial support of this work. D.Garcia-Gonzalez acknowledges support from the Talent Attraction grant (CM 2018 - 2018-T2/IND-9992) from the Comunidad de Madrid.

References

Alonso, L., Martínez-Hergueta, F., Garcia-Gonzalez, D., Navarro, C., García-Castillo, S. and Teixeira-Dias, F. (2020), "A finite element approach to model high-velocity impact on thin woven gfrp plates", *Int. J. Impact Eng.*, **142**. doi:10.1016/j.ijimpeng.2020.103593.

Alonso, L., Navarro, C. and Garc´ıa-Castillo, S. (2018a), "Analytical models for the perforation of thick and thin thicknesses woven-laminates subjected to high-velocity impact", *Compos. Part B* **143**, 292-300. doi:10.1016/j.compositesb.2018.01.030.

Alonso, L., Navarro, C. and García-Castillo, S. (2018b), "Experimental study of woven-laminates structures subjected to high-velocity impact". *Mech. Adv. Mater. Struct*., doi:10.1080/15376494.2018.1526354.

ASTM-Standard-D695-96 (1995), Standard test method for compressive properties of rigid plastics.

ASTM-Standard-D732-02 (2002), Standard test method for shear strenght of plastics by punch tool.

Bai, Y., Post, N., Lesko, J. and Keller, T. (2008), "Experimental investigations on temperature-dependent thermo-physical and mechanical properties of pultruded gfrp composites", *Thermochimica Apta*, **469**, 28-35. doi:10.1016/j.tca.2008.01.002.

Braun, O. and Naumovets, A. (2005), "Nanotribology: microscopic mechanisms of friction", *Surface science reports* **60**, 79-158. doi:10.1016/j.surfrep.2005.10.004.

Briescani, L., Manes, A. and Giglio, M. (2015), "An analytical model for ballistic impacts against plain-woven fabrics with a polymeric matrix", *Int. J. Impact Eng*., **78**, 138-149. doi:10.1016/j.ijimpeng.2015.01.001.

Buitrago, B., García-Castillo, S. and Barbero, E. (2010), "Experimental analysis of perforation of glass/polyester structures subjected to high-velocity impact". *Mater. Lett.*, **64**, 1052-1054. doi:10.1016/j.matlet.2010.02.007.

Chang, F. and Chang, K. (1987), "A progressive damage model for laminated composites containing stress concentrations", *J. Compos. Mater.*, **21**, 834-855. doi:10.1177/002199838702100904.

Chao Zhang, J., Sosa, C. And Bui, T. (2018), « meso-scale progressive damage modeling and life prediction of 3d braided composites under fatigue tension loading". *Compos. Struct*., **201**, 62-71. doi:10.1016/j.compstruct.2018.06.021.

Costas, M., Morin, D., Langseth, M., D´ıaz, J. and Romera, L. (2017), "Static crushing of aluminium tubes filled with pet foam and a gfrp skeleton. numerical modelling and multiobjective optimization", *Int. J. Mech. Sci*., **131-132**, 205-217. doi:10.1016/j.ijmecsci.2017.07.004.

Davila, C., Camacho, P. and Rose, C. (2005), "Failure criteria for frp laminates", *J. Compos. Mater*., **39**, 323-345. doi:https://doi.org/10.1177/0021998305046452.

Dhari, R., Patel, N., Wang, H. and Hazell, P. (2019), "Progressive damage modeling and optimization of fibrous composites under ballistic impact loading", *Mech. Adv. Mater. Struct.*, 1-18. doi:10.1080/15376494.2019.1655688.

Ding, G., Sun, L., Wan, Z., Li, J., Pei, X. and Tang, Y., 2018. "Recognition of damage modes and hilbert–huang transform analyses of 3d braided composites", *J. Compos. Sci.*, **2**, doi:10.3390/jcs2040065.

Ehsani, A. and Rezaeepazhand, J. (2016), "Stacking sequence optimization of laminated composite grid plates for maximum buckling load using genetic algorithm", *Int. J. Mech.Sci*., **119**, 97-106, 10.1016/j.ijmecsci.2016.09.028.

Ferguson, R., Hinton, M. and Hiley, M. (1998), "Determining the through-thickness properties of frp materials", *Compos. Sci. Technol*., **58**, 1411-1420. doi:10.1016/S0266-3538(98)00026-8.

García-Castillo, S., López-Puente, J., Sánchez Sáez, S., Barbero, E. and Navarro, C. (2006), "Analytical model for energy absorption capabilities of glass/polyester panels subjected to ballistic impact", *Conference in Developments in Theoretical and Applied Mechanics.*

García-Castillo, S., Sánchez-Sáez, S. and Barbero, E. (2012), "Influence of areal density on the energy absorbed by thin composite plates subjected to high-velocity impacts", *J. Strain Anal. Eng. Des*., **47**, 444-452. doi:10.1177/0309324712454996.

Garcia-Gonzalez, D., Rusinek, A., Jankowiak, T. and Arias, A. (2015), "Mechanical impact behaviour of polyetherether-ketone (peek)", *Compos. Struct.*, **124**, 88-99. doi:10.1016/j.compstruct.2014.12.061.

Garcia-Gonzalez, D., Zaera, R. and Arias, A. (2017), "A hyperelasticthermoviscoplastic constitutive model for semi-crystalline polymers: Application to peek under dynamic loading conditions", *Int. J. Plasticity*, **88**, 27-52. doi:10.1016/j.ijplas.2016.09.011.

Gil-Alba, R., Alonso, L., Navarro, C. and García-Castillo, S. (2019), "Morphological study of damage evolution in woven-laminates subjected to high-velocity impact", *Mech. Adv. Mater. Struct*., doi:10.1080/15376494.2019.1692264.

Guangyong, S., Tong, S., Chen, D., Gong, Z. and Li, Q. (2018), "Mechanical properties of hybrid composites reinforced by

carbon and basalt fibers", *Int. J. Mech. Sci.*, **148**, 636-651. doi:10.1016/j.ijmecsci.2018.08.007.

Haro, E., Odeshi, A. and Szpunar, J. (2016), "The energy absorption behavior of hybrid composite laminates containing nano-fillers under ballistic impact", *Int. J. Impact Eng*., **96**, 11-22. doi:10.1016/j.ijimpeng.2016.05.012.

Hashin, Z. (1980), "Failure criteria for unidirectional fiber composites", *J. Appl. Mech.*, **47**, 329-334. doi:10.1115/1.3153664.

Hazzard, M., Trask, R., Heisserer, U., Van Der Kamp, M. and Hallett, S. (2018), "Finite element modelling of dyneema® composites: from quasi-static rates to ballistic impact". *Compos. Part A: Appl. Sci. Manufact.*, **115**, 31-45. doi:10.1016/j.compositesa.2018.09.005.

Hongyong, J., Yiru, R., Binhua, G., Jinwu, X. and Fu-Gwo, Y., (2017), "Design of novel plug-type triggers for composite square tubes: enhancement of energy-absorption capacity and inducing failure mechanisms", *Int. J. Mach. Sci*., **113-136**, 636-651. doi:10.1016/j.ijmecsci.2017.06.050.

Hufenbach, W., Gude, M., B¨ohm, R.and Zscheyge, M. (2011), "The effect of temperature on mechanical properties and failure behaviour of hybrid yarn textile-reinforced thermoplastics". *Mater. Design*, **32**, 4278-4288. doi:10.1016/j.matdes.2011.04.017.

Kharazan, M., Sadr, M. and Kiani, M. (2014), "Delamination growth analysis in composite laminates subjected to low velocity impact", *Steel Compos. Struct*., **17**(4), 387-403. https://doi.org/10.12989/scs.2014.17.4.387.

Li, X., Nia, A., Ma, X., Yahya, M. and Wang, Z. (2017), "Dynamic response of kevlar 29/epoxy laminates under projectile impact–experimental investigation", *Mech. Adv. Mater. Struct.*, **24**, 114-121. doi:10.1080/15376494.2015.1107670.

Liu, P., Zhu, D., Wang, J. and Bui, T. (2017), "Structure, mechanical behavior and puncture resistance of grass carp scales". *J. Bionic Eng.*, **14**, 356-368. doi:10.1016/S1672-6529(16)60404-3.

Lopes, C., Camanho, P., G¨urdal, Z., Miamí, P. and González, E. (2009), "Low-velocity impact damage on dispersed stacking sequence laminates. part ii: Numerical simulations", *Compos. Sci. Technol.*, **69**, 937-947. doi:10.1016/j.compscitech.2009.02.015.

Mamivand, M. and Liaghat, G. (2010), "A model for ballistic impact on multi-layer fabric targets", *Int. J. Impact Eng*., **37**, 806-812. doi:10.1016/j.ijimpeng.2010.01.003.

Martínez-Hergueta, F., Ridruejo, A., Gonz´alez, C. and Llorca, J. (2015), "Deformation and energy dissipation mechanisms of needle-punched nonwoven fabrics: a multiscale experimental analysis", *Int. J. Solid. Struct*., **64-65**, 120-131. doi:10.1016/j.ijsolstr.2015.03.018.

Miamí, P., Camanho, P., Mayugo, J. and Dávila, C. (2007), "A continuum damage model for composite laminates: Part i–constitutive model", *Mech. Mater*., **39**, 897-908. doi:10.1016/j.mechmat.2007.03.005.

Moyre, S., Hine, P., Duckett, R., Carr, D. and Ward, I. (2000), "Modelling of the energy absorption by polymer composites upon ballistic impact", *Compos. Sci. Technol.*, **60**, 2631-2642. doi:10.1016/S0266-3538(00)00139-1.

Naik, N. and Doshi, A. (2005), "Ballistic impact behaviour of thick composites: analytical formulation", *AIAA J*., **43**, 1525-1536. doi:10.2514/1.11993.

Naik, N. and Shrirao, P. (2004), "Composite structures under ballistic impact", *Compos. Struct.*, **66**, 579-590. doi:10.1016/j.compstruct.2004.05.006.

Naik, N., Shrirao, P. and Reddy, C. (2006), "Ballistic impact behaviour of woven fabric composites: formulation", *Int. J. Impact Eng.,* **32**, 1521-1552. doi:10.1016/j.ijimpeng.2005.01.004.

Navarro, C. (1998), "Simplified modelling of the ballistic behaviour of fabric and fibre-reinforced polymer matrix composites", *Key Eng. Mater.*, **141-143**, 383-400.

Nguyen, T., Waldmann, D. and Bui, T. (2019), "role of interfacial transition zone in phase field modeling of fracture in layered heterogeneous structures", *J. Comput. Phys*., **386**, 585-610. doi:10.1016/j.jcp.2019.02.022.

Ou, Y., Zhu, D., Zhang, H., Huang, L., Yao, Y., Li, G. and Mobasher, B. (2016), "Mechanical characterization of the tensile properties of glass fiber and its reinforced polymer (gfrp) composite under varying strain rates and temperatures", *Polymers* **8**, doi:10.3390/polym8050196.

Pandya, K., Shaktivesh, H., Dowtham, H., Inani, A. and Naik, N. (2015), "Shear plugging and frictional behaviour of composites and fabrics under quasi-static loading", *Strain* **51**, 419-426. doi:10.1111/str.12153.

Pekbey, Y., Aslantas, K. and Yumak, N. (2017), "Ballistic impact response of kevlar composites with filled epoxy matrix", *Steel Compos. Struct.*, **24**, 191-200. https://doi.org/10.12989/scs.2017.24.2.191.

Potti, S. and Sun, C. (1997), "Prediction of impact induce penetration and delamination in thick composite laminates", *Int. J. Impact Eng.*, **19**, 31-48. doi:10.1016/S0734-743X(96)00005-X.

Rodriguez-Millan, M., Garcia-Gonzalez, D., Rusinek, A., Abed, F. and Arias, A. (2018), "Perforation mechanics of 2024 aluminium protective plates subjected to impact by different nose shapes of projectiles", *Thin-Wall. Struct.*, **123**, 1-10. doi:10.1016/j.tws.2017.11.004.

Saberi, H., Bui, T., Furukawa, A., Rahai, A. and Hirose, S. (2020), "frp-confined concrete model based on damage-plasticity and phase-field approaches", *Compos. Struct.*, **240**, doi:10.1016/j.compstruct.2020.112263.

Scazzosi, R., Manes, A. and Giglio, M. (2019), "Analytical model of high-velocity impact of a deformable projectile against textilebased composites", *J. Mater. Eng. Perform*., **28**. doi:10.1007/s11665-019-04026-x.

Shaoquan, W., Shangli, D., Yu, G. and Yungang, S. (2017), "Thermal ageing effects on mechanical properties and barely visible impact damage behavior of a carbon fiber reinforced bismaleimide composite", *Mater. Design*, **115**, 213-223. doi:10.1016/j.matdes.2016.11.062.

Sikarwar, R. and Velmurugan, R. (2019), "Impact damage assessment of carbon fiber reinforced composite with different stacking sequence", *J. Compos. Mater*., doi.org/10.1177/0021998319859934.

Smith, J., F.L., M. and Schiefer, H. (1958), "Stress-strain relationships in yarns subjected to rapid impact loading:5. wave propagation in long textile yarns impacted transversally", *J. Res. National Bureau of Standars,* **60**, 517–534.

Tarfaoui, M., Choukri, S. and Neme, A. (2008), "Effect of fibre orientation on mechanical properties of the laminated polymer composites subjected to out-of-plane high strain rate compressive loadings", *Compos. Sci. Technol.*, **68**, 477-485. doi:10.1016/j.compscitech.2007.06.014.

Turon, A., D´avila, C., Camaho, P. and Coste, J. (2007), "An engineering solution for mesh size effects in the simulation of delamination using cohesive zone models", *Eng. Fract. Mech*., **74**, 1665-1682. doi:10.1016/j.engfracmech.2006.08.025.

Wen, H. (2000), "Predicting the penetration and perforation of frp laminates struck normally by projectiles with different nose shapes", *Compos. Struct.*, **49**, 321-329. doi:10.1016/S0263-8223(00)00064-7.

Wen, H. (2001), "Penetration and perforation of thick frp laminates", *Compos. Sci. Technol.*, **51**, 1163-1172. doi:10.1016/S0266-3538(01)00020-3.

Xiao, J., Gama, B. and Gillespie Jr, J. (2007), "Progressive damage and delamination in plain weave s-2 glass/sc-15 composites under quasi-static punch-shear loading", *Compos. Struct.*, **78**, 182-196. doi:10.1016/j.compstruct.2005.09.001.

Yiru Ren, H., Zhang, S., Liu, Z. and Nie, L. (2018), "Multiscale finite element analysis for tension and ballistic penetration damage characterizations of 2d triaxially braided composite", *J. Mater. Sci.*, **53**, 10071-10094. doi:10.1007/s10853-018-2248-x.

Zhang, X., Liu, T., He, N. and Jia, G. (2016), "Investigation of two finite element modelling approaches for ballistic impact response of composite laminates", *Int. J. Crashrothiness*, **22**, 377-393. doi:10.1080/13588265.2016.1270495.

Zhu, G., Goldsmith, W. and Dharan, C. (1992), "Penetration of laminated kevlar by projectiles ii. analytical model", *Int. J. Solid. Struct.*, **29**, 421-436. doi.org/10.1016/0020-7683(92)90208-B.

Zhu, G., Sun, G., Yu, H., Li, S. and Li, Q. (2018), "Energy absorption of metal, composite and metal/composite hybrid structures under oblique crushing loading", *Int. J. Mech. Sci.*, **135**, 458-483. doi:10.1016/j.ijmecsci.2017.11.017.

CC